WATER RESOURCES RESEARCH, VOL. 50, 580–600, doi:10.1002/2013WR013763, 2014

A copula-based precipitation forecasting model: Investigating the interdecadal modulation of ENSO's impacts on monthly precipitation

C. Prakash Khedun,[1] Ashok K. Mishra,[2] Vijay P. Singh,[1,3,4] and John R. Giardino[1,5]

Received 1 March 2013; revised 9 November 2013; accepted 13 November 2013; published 27 January 2014.

[1] The influence of two large-scale circulation patterns (the El Niño Southern Oscillation (ENSO) and the Pacific Decadal Oscillation (PDO)), and the effect of the interdecadal modulation of ENSO on precipitation in the state of Texas, U.S., was explored. Texas, by virtue of its size, topography, and geographical location, spans a wide range of climatic regions. The state is divided into 10 climate divisions. The precipitation pattern in each division follows different probability distributions. The climate regimes which trigger this difference are discussed. The seasonal correlation between ENSO and PDO with precipitation anomaly in each climate division was established. Copula-based models were developed to examine the dependence structure between the large-scale climate indices and average monthly seasonal precipitation. The choice of copula is discussed in light of the dependence structure. The selected copulas were then used to simulate precipitation anomalies in three climate divisions: one which has a semiarid climate, one located in the wettest region, and one straddling the subtropical humid and subtropical subhumid regions of the state. The statistical performance of bivariate models for ENSO and precipitation, and trivariate models for ENSO, PDO, and precipitation, in simulating precipitation anomalies were compared. In general, inclusion of PDO was found to improve simulation results. The most notable improvement was in simulating negative precipitation anomalies during La Niña and negative PDO. The copula models were also tested for their abilities to predict precipitation anomalies in these three regions. Again, the trivariate models performed better, especially in predicting droughts due to La Niña and negative PDO.

Citation: Khedun, C. P., A. K. Mishra, V. P. Singh, J. R. Giardino (2014), A copula-based precipitation forecasting model: Investigating the interdecadal modulation of ENSO's impacts on monthly precipitation, *Water Resour. Res.*, *50*, 580–600, doi:10.1002/2013WR013763.

1. Introduction

[2] Large-scale circulation patterns are known to have a noticeable influence on precipitation around the globe. *Ropelewski and Halpert* [1986] identified regions of coherent response and associated phases between precipitation and temperature patterns with respect to El Niño Southern Oscillation (ENSO) episodes in North America. *Kurtzman and Scanlon* [2007] found a significant increase (decrease) in precipitation with respect to El Niño (La Niña) in southern and central U.S. Correlation of precipitation with the Pacific Decadal Oscillation (PDO) was found to be weaker, but it nonetheless influences precipitation patterns, especially when the two phenomena are evolving in the same phase. On the other side of the Pacific Ocean, the Interdecadal Pacific Oscillation (IPO), in conjunction with other climate variability patterns including ENSO, have been found to affect the trends in annual maximum streamflow [*Ishak et al*., 2013]. Higher flood risks have been associated with persistent periods of negative IPO. Thus, monitoring the state of IPO can help forewarn potential flood risks [*Pui et al*., 2011].

[3] It has been shown that PDO modulates the effect of ENSO; El Niño (La Niña) during the positive (negative) phase of PDO leads to stronger climate responses than when they are evolving in opposite phases [*Gershunov and Barnett*, 1998]. Others, however, argue that stronger El Niño and La Niña events are a result of the random decadal variation of ENSO and may even be responsible for the PDO [*McPhaden et al*., 2006; *Rodgers et al*., 2004].

[4] Nonetheless, *McCabe and Dettinger* [1999] state that precipitation prediction skills in North America can be enhanced when information on both ENSO and PDO are considered. The ability to forecast precipitation with sufficient lead time and a reasonable degree of accuracy, given the projected state of large-scale circulation patterns, can be extremely valuable for short-term water resources

[1]Water Management and Hydrological Science, Texas A&M University, College Station, Texas, USA.
[2]Glenn Department of Civil Engineering, Clemson University, Clemson, South Carolina, USA.
[3]Department of Biological and Agricultural Engineering, Texas A&M University, College Station, Texas, USA.
[4]Zachry Department of Civil Engineering, Texas A&M University, College Station, Texas, USA.
[5]Department of Geology and Geophysics, Texas A&M University, College Station, Texas, USA.

Corresponding author: C. P. Khedun, Water Management and Hydrological Science, 321E Scoates Hall, MS 2117, Texas A&M University, College Station, TX 77843, USA. (pkhedun@tamu.edu)

0043-1397/14/10.1002/2013WR013763

planning and to mitigate the devastating effect of droughts. A wide range of tools and methods have been developed to predict precipitation, streamflow, drought indices, and other hydrologic variables [e.g., *Chowdhury and Sharma*, 2009; *Devineni et al*., 2008; *Grantz et al*., 2007].

[5] In this study, a statistical model is developed to assess (i) how well ENSO conditions alone can forecast monthly precipitation, and (ii) if considering both the state of ENSO and PDO improves precipitation prediction in the state of Texas. Texas is the appropriate setting for this analysis as it covers a large area and is subject to a range of climate—from tropical humid and hurricane prone on the east side to desert on the west part, with an intermediate subhumid tropical region. It cycles through short- and long-duration droughts, interspersed with periods of above average precipitation. Precipitation, or the lack thereof, has often been linked to conditions in the Pacific Ocean [*Ropelewski and Halpert*, 1986]. The state of ENSO is a major determinant: El Niño often leads to above average precipitation and La Niña has been associated with major droughts in the state. Further, PDO has also been shown to affect local climatic conditions. *Özger et al*. [2009], for example, using two Niño indices and a PDO index, showed that there is a robust relationship between large-scale circulation patterns and the Palmer Drought Severity Index (PDSI). The correlation structure was not uniform across the state; the semiarid regions exhibited higher correlation than the subtropic regions. *Mishra et al*. [2011], using cross-correlation and cross-wavelet analysis, showed that the maximum cross-correlation as well as the spatial correlation, between the Niño 3.4 index, Southern Oscillation Index (SOI), and PDO with streamflow in Texas varies from season to season. Winter streamflow extremes were most influenced by SOI.

[6] This study employs copulas to model the dependence between ENSO, PDO, and precipitation, since they each exhibit different marginal behavior. Copulas have been effectively used to determine the conditional probabilities and return periods of drought events during different ENSO states [*Wong et al*., 2010]. *Maity and Nagesh Kumar* [2008] modeled the dependence of two climate variables (ENSO and the Equatorial Indian Ocean Oscillation (EQUINOO)) combined into a joint predictor with the Indian Summer Monsoon using copulas, and were able to predict rainfall at one station with a high degree of confidence. To our knowledge, a more complex framework with two predictors (in this case, the state of ENSO and PDO) and precipitation as response variable has not been investigated.

[7] The study was divided into the following main sections. The correlation between ENSO and PDO on precipitation in the 10 climate divisions in Texas were first assessed separately. The interdecadal modulation of ENSO by PDO and its effect on precipitation was then examined. Probability distributions were then fitted to the climate indices data and to precipitation anomalies in each climate division. The choice of marginals, with respect to basic statistical characteristics of precipitation is discussed. Bivariate copula models for ENSO and precipitation, and trivariate models for ENSO, PDO, and precipitation, were developed and compared. The choice of copulas is discussed in light of the dependence structure. The selected copula was then used to simulate precipitation in three climate divisions: one which has a semi-arid climate; one located in the wettest region; and one in the middle, straddling the subtropical humid and subtropical subhumid regions of the state. Two models, a bivariate, using ENSO and precipitation, and a trivariate, using ENSO, PDO, and precipitation, were constructed and compared. Using the most appropriate copula, precipitation anomalies in these three distinctly different climate divisions were simulated using both models and the statistics of the simulated values were compared with the observations. The copula models were also tested for their abilities to predict precipitation anomalies in these three regions.

[8] The paper is structured as follows. Section 2 describes the study area, which is divided into 10 climate divisions, and explains how and why the climate changes across the state. Section 3 describes the data set for precipitation and climate indices, and section 4 explains the methodology adopted in this study. In section 5, the influence of ENSO and PDO on precipitation in each climate division is established and a detailed illustration of how the copula model was developed and validated is provided, followed by the results and discussion on precipitation simulation and forecasting. Physical reasons that explain the marginal and copula selection are also given. The conclusions drawn from this study are presented in section 6.

2. Study Area

[9] The state of Texas is the second largest state, with a total land and inland water area of 691,146 km^2, and the second most populous (25.67 million in 2012), in the U.S. It extends from latitude 25°50′N to 36°30′N and from longitude 93°31′W to 106°38′W. It has a mean elevation of 519 m; the highest point is the Guadalupe Peak (2668 m), on the far western part of the state, and the lowest point is the Gulf of Mexico (sea level), which also forms the southeastern boundary. By virtue of its size, topography, and geographical location, Texas spans a wide range of climatic regions with a multitude of microclimates [*Nielsen-Gammon*, 2009]. The eastern third of the state is classified as subtropical humid and the middle third as subtropical subhumid and subtropical steppe, while the western region is subtropical arid and the north western panhandle area is continental steppe (Figure 1). On the Köppen-Geiger climate classification system (not shown here), the eastern half of the state is warm temperate, fully humid, with hot summer (Cfa) while the western half is mostly cold arid steppe (BSk). The far western tip is arid desert (BWk) and eastern lower edge, running along the border with Mexico, is arid steppe, with hot arid temperatures (BSh).

2.1. Climate Divisions

[10] The number and areal extent of climate divisions in the state of Texas has undergone several iterations; in 1904, the state had seven climatic divisions, which was reduced to three in 1936, and in 1951, the state was divided into the current 10 climatic regions (Figure 1) [*Griffiths et al*., 1990]. One limitation of the current climate division is that it does not always reflect homogeneous climate regions, but has geographical boundaries that match county boundaries. Furthermore, they are not of equal area;

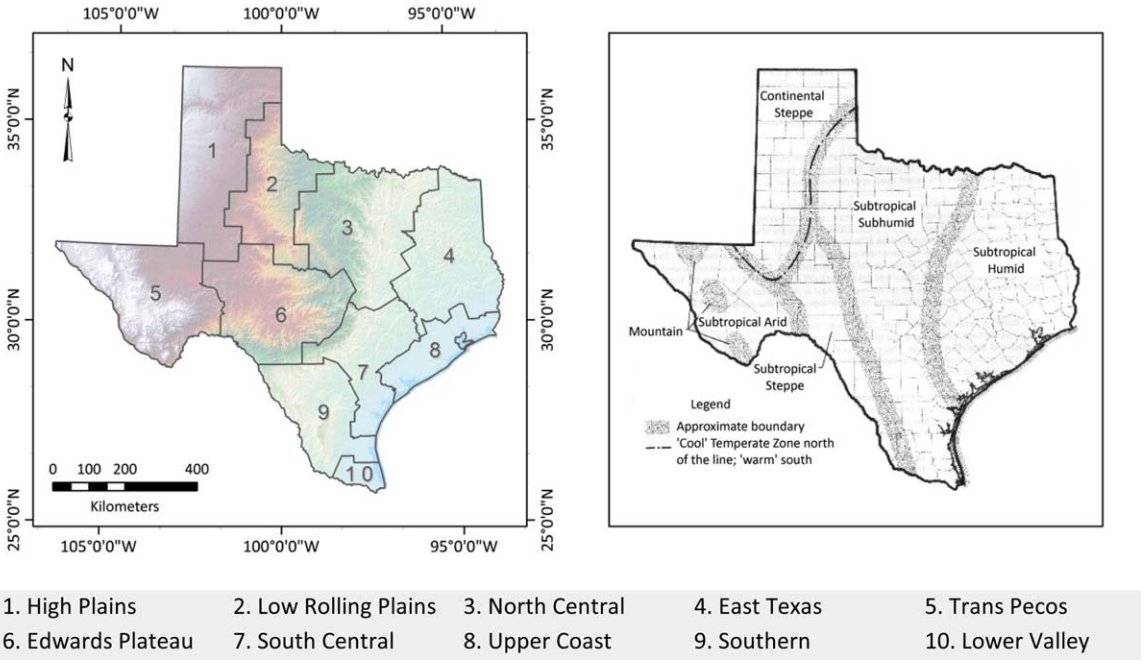

Figure 1. Climate divisions and climate regions (*Larkin and Bomar* [1983]) of Texas.

climate division 1 is the largest, covering nearly 15% of the state, and division 10 is the smallest and covers just over 1%.

2.2. Precipitation Pattern

[11] The average annual precipitation in the state decreases longitudinally from east (1535 mm at Beaumont) to west (247 mm at El Paso) at a rate of 100 mm/°longitude. Violin plots of monthly precipitation in each climate division are shown in Figure 2. A violin plot is a boxplot combined with kernel density plots, added on each side of the boxplot, to show the probability distribution of the data set. Moving from west to east/southeast across the state, along with an increase in the median value, more dispersion and skewness is noted in the monthly precipitation. Furthermore, the probability of months with zero precipitation is highest for climate divisions 1 and 5 and lowest for divisions 4 and 8.

[12] The mean monthly precipitation in each climate division, along with that for the whole state, is given in Figure 3. Texas has a very distinct bimodal precipitation pattern; in fact precipitation patterns in climate divisions located in the subtropical subhumid and subtropical steppe part of the state (2, 3, 6, 7, and 9) are bimodal, prompting a bimodal pattern for the state. May is the wettest month followed by September. Climate divisions 1 and 5, located in the continental steppe and subtropical arid zones, respectively, have a unimodal precipitation pattern; November^{0}–April^{+} is the dry season and May^{0}–October^{0} is the wet season. Wet season rainfall represents 75% of annual precipitation. High precipitation in July and August is the consequence of the North American Monsoon (NAM),

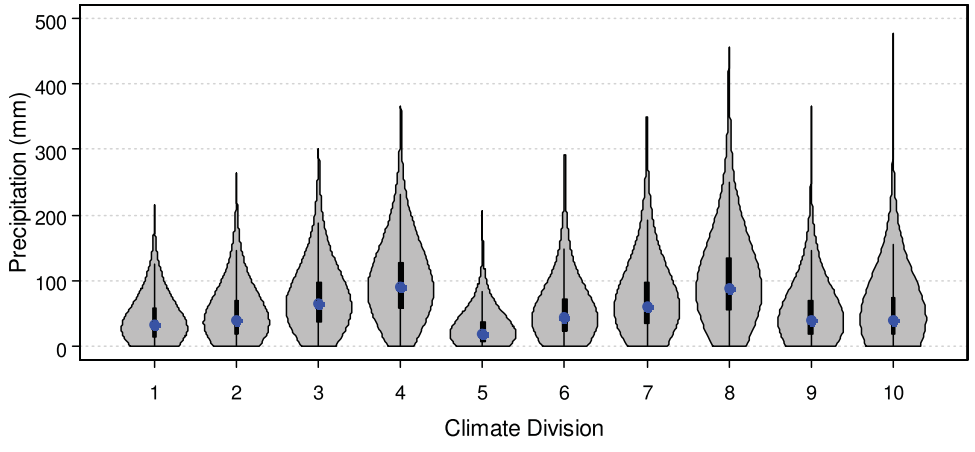

Figure 2. Violin plots of monthly precipitation in each climate division in Texas. Thick black line and blue dot shows the 25th and 75th percentile range and median, respectively, and thin black line shows the 5th and 95th percentile range.

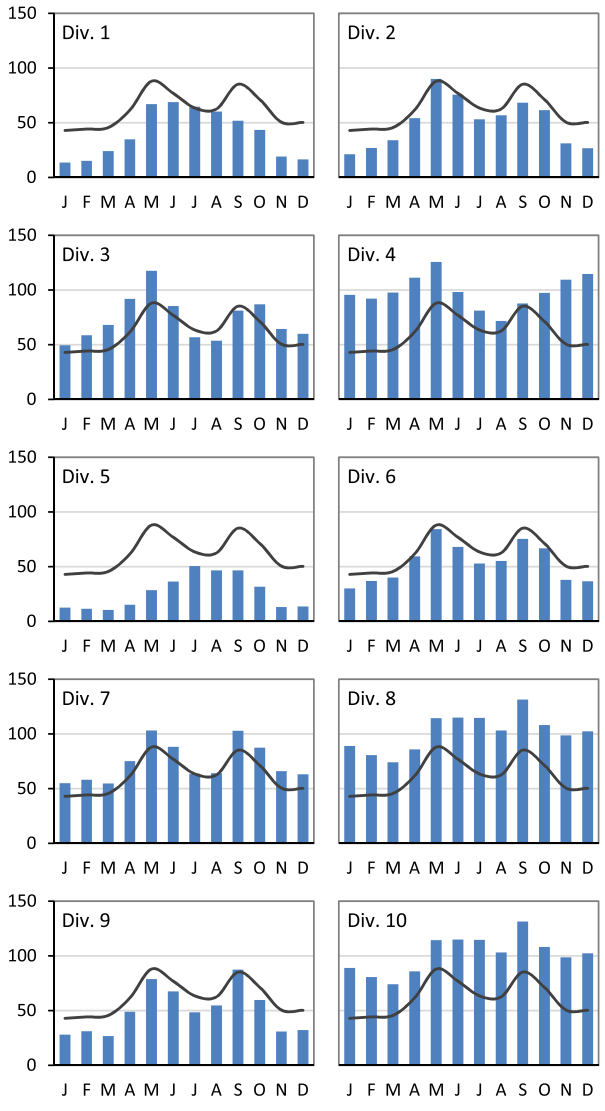

Figure 3. Mean monthly precipitation (in mm) in each climate division based on data for 1900–2011. Solid black line represents the monthly mean precipitation for the whole state.

which can dramatically change the landscape of the arid southwestern U.S. NAM is triggered by differential warming between land and the Pacific Ocean, causing the monsoon ridge to migrate north and result in a shift in wind direction from southwesterly to more southeasterly, marking the onset of NAM. Precipitation is due to low level moisture surges, carried from the Gulf of California, and slow upper-level moisture from the Gulf of Mexico. Interannual variability in the monsoon rainfall is not strongly associated with ENSO [*Adams and Comrie*, 1997]. However, El Niño (La Niña) occurring concurrently with high (low) phase of the North Pacific oscillation causes a weaker (stronger) and southward (northward) displaced monsoon ridge. Such condition delays (advances) the onset of NAM and below (above) average early summer precipitation is recorded [*Castro et al.*, 2001]. Climate division 1 is affected by NAM, but May and June precipitations are the highest due to the West Texas Dryline [*Nielsen-Gammon*, 2009]. The dryline is a result of collision between warm dry air from the desert west and moisture laden air from the Gulf of Mexico, causing severe thunderstorm on the east of the dryline. The dryline disappears in the summer as the jet stream weakens and the monsoon system arises.

[13] The eastern, coastal, climate divisions 4, 8, and 10 have almost uniform monthly mean precipitation, fueled by a constant supply of moisture from the Gulf of Mexico and occasional hurricanes in the summer, which can bring considerable amount of rainfall in a short period of time.

3. Data

3.1. Precipitation

[14] Sparse weather records in Texas exist from as early as 1836, but statewide weather records began in 1895. The time period considered in this study is January 1900 to March 2012. Monthly mean precipitation data for each of the 10 climate divisions in Texas was obtained from the National Climatic Data Center (NCDC). The monthly values are equal-weighted averages from stations reporting both temperature and precipitation within a division. Equal weightage minimizes any bias that may result from changes in the number of stations included over time [*Guttman and Quayle*, 1996]. Figure 4 gives a plot of monthly precipitation for each division, smoothed with a 13 month centered moving average window, around the long-term means for the data set.

3.2. Climate Indices

3.2.1. Southern Oscillation Index (SOI)

[15] ENSO is a coupled ocean-atmosphere phenomenon associated with changes in the sea surface temperature in the tropical Pacific and major shifts in the Intertropical Convergence Zone over the Pacific Ocean. The Southern Oscillation is the atmospheric component, pertaining to the large-scale fluctuation in atmospheric mass between the Indian and Pacific Oceans in the tropics and subtropics [*Trenberth*, 1984]. SOI combines the fluctuations in atmospheric pressure between Tahiti (17.5°S, 149.6°W) and Darwin, Australia (12.4°S, 130.9°E) into one series. Monthly SOI data (standardized Tahiti − standardized Darwin), derived following *Trenberth* [1984], was obtained from the National Center for Atmospheric Research (NCAR) Climate & Global Dynamics (CGD) climate analysis section. *Trenberth*'s [1984] standardization maximizes the signal-to-noise ratio. SOI is preferred to other ENSO indices (e.g., Niño indices) for this study as they exhibit slightly higher correlations with precipitation (K. Redmond, Classification of El Niño and La Niña Winters, available at http://www.wrcc.dri.edu/enso/ensodef.html).

[16] The correlation between SOI and precipitation in the southern U.S. is generally negative. Negative correlations, however, affect the types of copulas that can be employed in this study, as some copulas, e.g., the Archimedean copula families, exist in the positive dependence space. Rotated versions of these copulas can be used to cover negative dependence, but would nearly double the number of copulas to be included in the analysis. To circumvent this hurdle, we created a negative SOI series (NSOI) by multiplying the SOI values by −1. A plot of monthly NSOI values is shown in Figure 5. El Niño and La

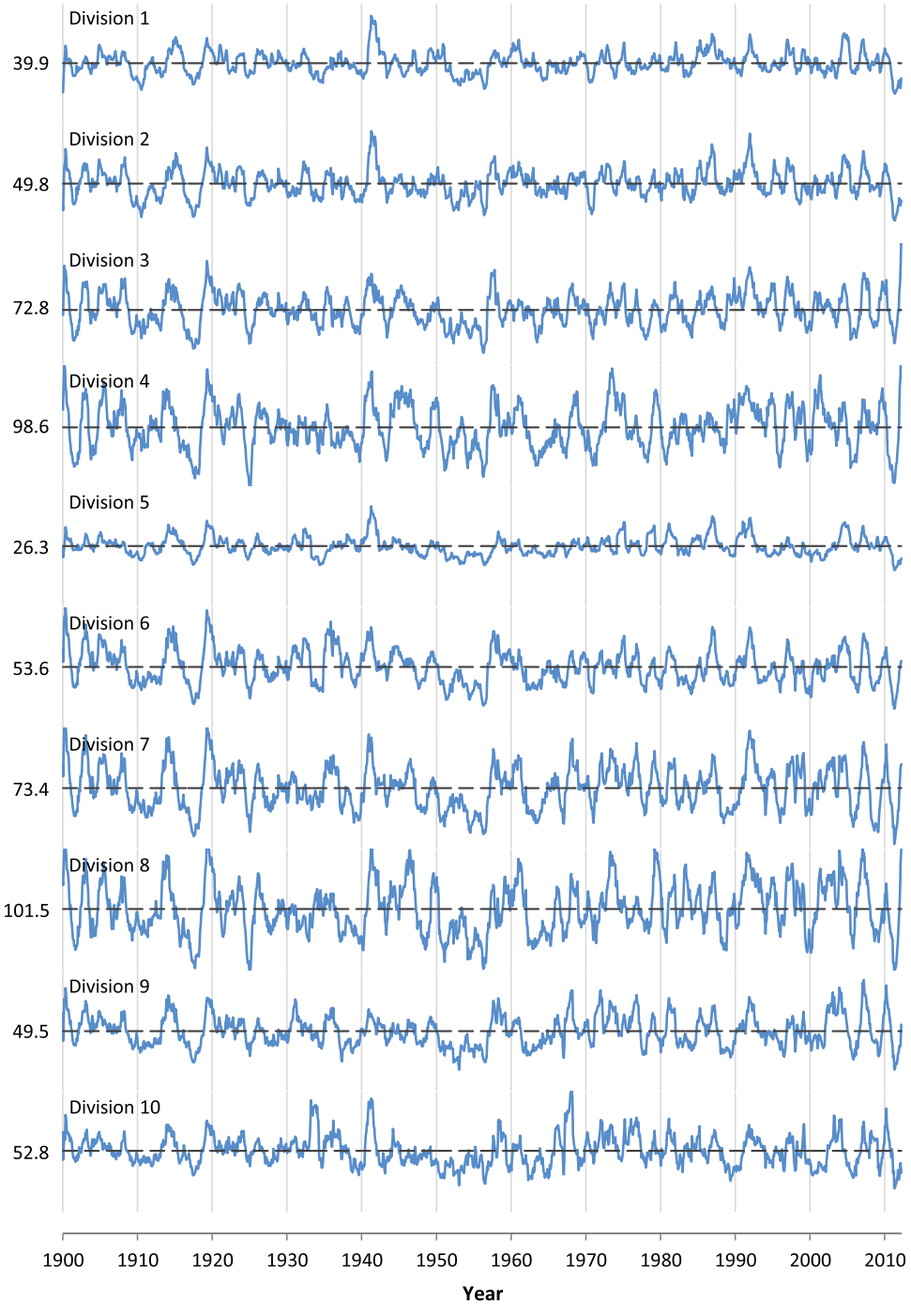

Figure 4. Time series of monthly precipitation for each climate division. The time series has been smoothed with a 13 month centered running mean filter. The dotted line represents the means for the data set (mm). The time series were not padded at the ends.

Niña events are associated with extremes in the NSOI series. Unlike with the Niño 3.4 index (North American countries reach consensus on El Niño definition, available at http://www.noaanews.noaa.gov/stories2005/s2394.htm), there is no established definition for ENSO events based on SOI. *Ropelewski and Jones* [1987] suggested that ENSO events can be identified using a 5 month running mean of NSOI values, with El Niño (La Niña) defined when the running mean value is above +0.5 (below −0.5) standard deviations for 5 months or longer. *Kiladis and van Loon* [1988], on the other hand, suggested that ENSO events be defined when both Sea Surface Temperature (SST) is at least 0.5°C above mean for three seasons and SOI is negative and below −1 for the same duration. The plot in Figure 5 shows a 5 month running mean and the ±0.5 and ±1 thresholds overlain on monthly NSOI indices.

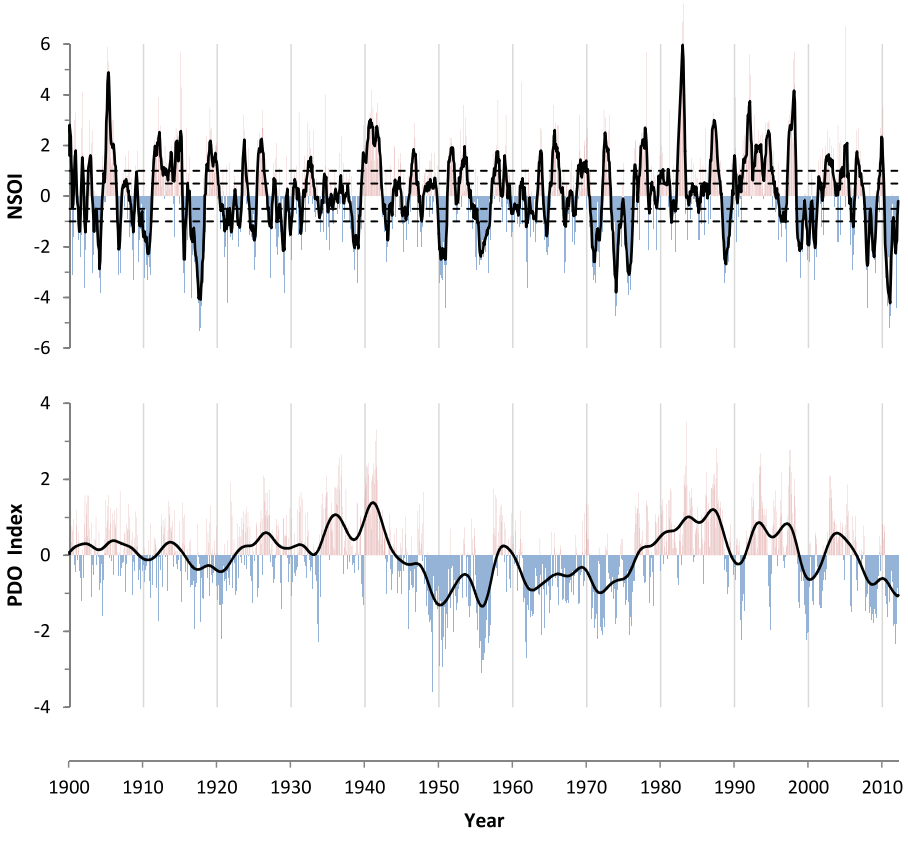

Figure 5. Time series of monthly NSOI and PDO index. The NSOI series is overlain with a 5 month centered running mean filter and ±0.5 and ±1 thresholds. The PDO series is smoothed with 10 passes of a 13 month centered running mean filter. The time series were not padded at the ends.

3.2.2. Pacific Decadal Oscillation (PDO)

[17] Monthly PDO indices for the study period were obtained from the Joint Institute for the Study of the Atmosphere and Ocean (JISAO). The PDO index is the leading principal component from an un-rotated empirical orthogonal analysis of monthly residuals of the North Pacific Ocean Sea Surface Temperature Anomaly (SSTA), poleward of 20°N [*Mantua et al*., 1997]. The residuals are the difference between observed anomalies and monthly mean global average SSTA; hence the index is not affected by global warming trends.

[18] Figure 5 gives a plot of the monthly PDO indices. The series was smoothed with a centered 13 month moving average filter to highlight multidecadal frequencies. Positive (negative) values indicate warm (cold) phases of PDO. Between January 1900 and March 2012, 51.4% of the record was warm months and 48.4% was cold months. There have been two full PDO cycles in the last century: cool phases lasting from 1890 to 1924 and from 1947 to 1976, and warm phases lasting from 1925 to 1946 and from 1977 to 1998 [*Mantua and Hare*, 2002; *Minobe*, 1997]. From 1998, the PDO has been in a short 4 year cold phase until 2002, a warm phase lasting from 2002 to 2007, and is currently in a cold phase.

4. Methodology

[19] The influence of climate variability patterns on precipitation was examined using Pearson correlation. Probability distribution functions were fitted to NSOI, PDO, and precipitation. Copulas were used to model the relationship between climate indices and precipitation.

4.1. Correlation of ENSO and PDO With Precipitation

[20] Pearson correlation was used to determine the relationship between climate variability patterns and gauged seasonal precipitation in each climate division. The correlation coefficient can be used as a statistical test of independence to help make inferences about the degree of association between variables. The magnitude and sign of the correlation coefficient indicate the existence, strength, and nature of any association [*Redmond and Koch*, 1991].

4.2. Copula Selection

[21] Simulating and predicting the influence of large-scale circulation phenomena on precipitation requires multidimensional modeling of random variables. Multidimensional analyses have traditionally been expressed using classical multivariate families which assume that the marginals describing the behavior of the individual random variables are from the same family as the multivariate distributions. Moreover, the dependence structure of most conventional multivariate distributions directly or indirectly assumes linear correlation given through Pearson's product-moment correlation coefficient (e.g., bivariate gamma distributions discussed by *Yue et al*. [2001]). A copula, which is due to *Sklar* [1959], skirts these constraints and allows univariate margins and dependence structure to be modeled independently.

[22] A copula is a multivariate distribution with all univariate margins being standard uniform $[U(0,1)]$. *Joe* [1997] explains that for an m-variate distribution $F \in \mathcal{F}(F_1, \ldots, F_m)$, with jth univariate margin F_j, there exists a copula $C : [0,1]^m \rightarrow [0,1]$ that satisfies

$$F(x) = C[F_1(x_1), \ldots, F_m(x_m)], \quad x \in \Re^m \tag{1}$$

[23] If F is a continuous m-variate distribution function with univariate margins $F_1, \ldots, F_m$, and quantile functions $F_1^{-1}, \ldots, F_m^{-1}$, then

$$C(\boldsymbol{u}) = F\left[F_1^{-1}(u_1), \ldots, F_m^{-1}(u_m)\right] \tag{2}$$

is unique; otherwise C is uniquely determined on $RanF_1 \times \ldots \times RanF_m$, where $RanF_j = F_j([-\infty, \infty])$ is the range of F_j.

[24] The copula C can be considered "independent" of the univariate margins, then

$$G(\boldsymbol{y}) = C[G_1(y_1), \ldots, G_m(y_m)] \tag{3}$$

is a distribution function if $G_1, \ldots, G_m$ are all univariate distribution functions. The copula can be parametrized by a single value θ, or can be multi-parameter.

[25] Copulas are generally classified into four classes: Archimedean, extreme value, elliptical, and other miscellaneous class. In this study, bivariate and trivariate cases of two copulas from the elliptical class (Gaussian and Student's t with different degrees of freedom) and eight from the Archimedean class (Clayton, Gumbel, Frank, Joe, BB1, BB6, BB7, and BB8) were considered. BB1, BB6, BB7, and BB8 are from the two-parameter families. The two-parameter families of copula can be particularly useful in capturing more than one type of dependence, e.g., one parameter for upper tail and lower tail dependence each, or one parameter for concordance while the other captures the lower tail dependence [*Joe*, 1997].

4.2.1. Marginal Distribution Selection

[26] Marginals were chosen from a suite of theoretical probability distributions commonly used in hydrology. A combination of graphical assessment, Q-Q plots, and formal goodness-of-fit techniques were used to compare observed sample distributions with theoretical distributions in the selection of the best fitting marginal.

[27] The chi-square goodness-of-fit test was used in order to discriminate between theoretical distributions. The chi-square goodness-of-fit test verifies the null hypothesis that the data follows the specified distribution. The test statistic is given by:

$$\chi^2 = \sum_{i=1}^{k} \frac{(O_i - E_i)^2}{E_i} \tag{4}$$

where O_i is observed frequency for bin i, E_i is the expected frequency for bin i, and k is the total number of bins based on Sturges' formula $(k = \log_2 N + 1)$. $E_i = N(F(Y_u) - F(Y_l))$, where F is the cumulative distribution function for the distribution under test, Y_u and Y_l are, respectively, the upper and lower limits for class i, and N is the sample size. The test statistic is distributed as a χ^2 random variable with $k - p - 1$ degrees of freedom, p being the number of estimated parameters. The test fails to reject the null hypothesis when χ^2 is less than the chi-square critical value with $k - p - 1$ degrees of freedom and significance level α.

4.2.2. Elliptical Copula

4.2.2.1. Gaussian (Normal) Copula

[28] The Gaussian copula, derived from a multivariate Gaussian distribution, is perhaps the most popular copula. It can be expressed as

$$C_\Sigma(u_1, \ldots, u_m) = \boldsymbol{\Phi}_\Sigma[\Phi^{-1}(u_1), \ldots, \Phi^{-1}(u_m)] \tag{5}$$

where Φ is the distribution function of a standard normal variable $N(0,1)$ and $\sum$ is the correlation matrix with $m(m-1)/2$ parameters satisfying the positive semidefiniteness constraint. $\boldsymbol{\Phi}_\Sigma$ is the m-variate standard normal distribution with mean 0 and covariance matrix $\sum$, i.e., $\boldsymbol{\Phi}_\Sigma \sim N_m(0, \Sigma)$ [*SAS/ETS*, 2011].

4.2.2.2. Student's *t* Copula

[29] The Student's t copula can be written as

$$C_\Theta(u_1, \ldots, u_m) = \boldsymbol{t}_{v,\Sigma}[t_v^{-1}(u_1), \ldots, t_v^{-1}(u_m)] \tag{6}$$

where $\Theta = \left\{(v, \Sigma) : v \in (1, \infty), \Sigma \in \mathbb{R}^{m \times m}\right\}$ and t_v is the univariate t distribution with v degrees of freedom. $\boldsymbol{t}_{v,\Sigma}$ is the multivariate Student's t distribution with correlation matrix $\sum$ and v degrees of freedom [*SAS/ETS*, 2011].

4.2.3. Archimedean Copulas

[30] The Archimedean family is the most popular copula family employed in hydrological analyses because of its ease of construction and wide range of choices for the strength of dependence. The general form of the Archimedean family is

$$C(u_1, \ldots, u_m) = \phi^{-1}[\phi(u_1) + \cdots + \phi(u_m)] \tag{7}$$

where $\phi : [0,1] \rightarrow [0, \infty)$ is a strict Archimedean copula generator function and its inverse ϕ^{-1} is completely monotonic on $[0, \infty)$. The generator is a decreasing function and is termed strict, and the resulting copula a strict copula, when $\phi(0) = \infty$ and $\phi(1) = 0$ [*SAS/ETS*, 2011]. The dependence parameter θ is embedded in the generating function ϕ.

4.2.4. Copula Parameter Estimation

[31] The copula parameter can be estimated via several methods: the exact maximum likelihood method, the moment-like method, which is based on the inversion of the nonparametric dependence measure (e.g., Kendall's tau), and the maximum pseudo-likelihood method [*Chowdhary et al.*, 2011]. The first method can be used if the marginal distributions are already uniform. The last two methods require that the observations, $\boldsymbol{x}_i = (x_{i1}, \ldots, x_{im})^\top$, $i = 1, \ldots, n$, are transformed into pseudo-observations, $\hat{\boldsymbol{u}}_i = (\hat{u}_{i1}, \ldots, \hat{u}_{im})$, $i = 1, \ldots, n$, i.e., in the unit hypercube. $\hat{u}_{i,j} = (1/(n+1))rank\ (x_{i,j})$, where $rank\ (x_{i,j})$ is the rank, in ascending order between $i = 1, \ldots, n$. Nonparametrically ranking the joint variates through their respective scale ranks ensures that the dependence structure is determined independently of the marginals [*Genest and Favre*, 2007]. In this study, the maximum pseudo-likelihood method was used. Another appealing advantage of this method is that it yields smaller mean squared errors [*Chowdhary et al.*, 2011]. For a copula $C(u_1, \ldots, u_m; \theta)$, with density $c(u_1, \ldots, u_m; \theta)$, the parameter θ can be estimated by maximum likelihood:

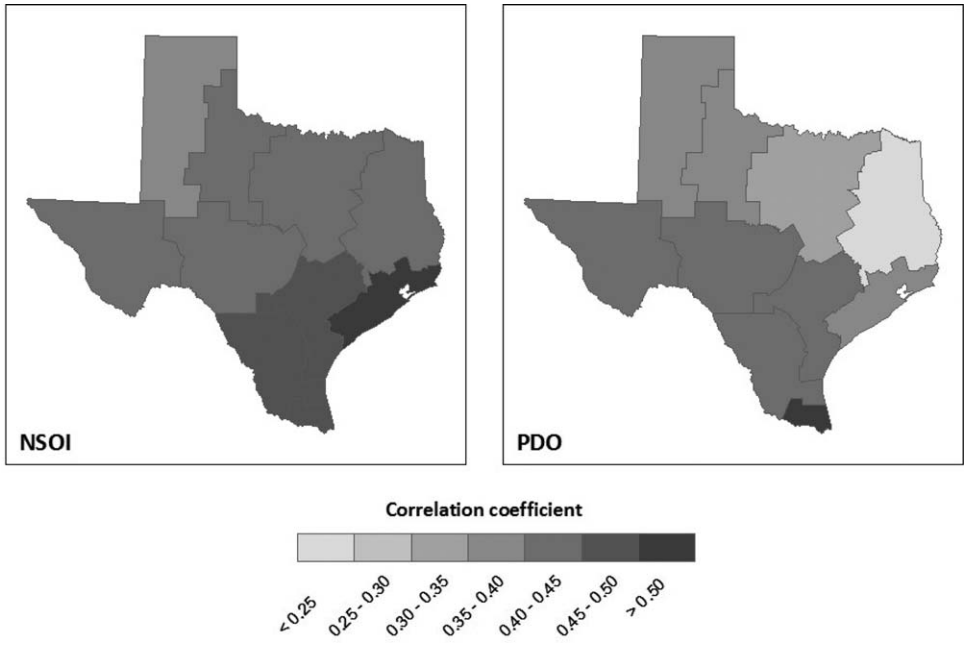

Figure 6. Plots of correlation coefficients between average June^0–November^0 NSOI and mean cold season (October^0–March$^+$) precipitation anomalies and average cold season PDO index and mean cold season precipitation anomalies.

$$\hat{\theta} = \arg\max_{\theta\in\Theta} \sum_{i=1}^{n} \log c(\hat{u}_{i1}, \ \ldots, \hat{u}_{im}; \theta) \tag{8}$$

4.2.5. Goodness-of-Fit Tests

[32] A combination of graphical and formal goodness-of-fit tests was employed to select the most suitable copula. A scatter plot of observed data (the support of the empirical copula C_m) overlapped upon a set of random samples generated from copula C_{θ_m} is an efficient way of visually comparing the effectiveness of the fitted copula in capturing the dependence structure in the empirical data set. *Genest and Favre* [2007] suggest that in order to avoid any arbitrariness due to sampling variability, a large sample generated from C_{θ_m} is preferred to smaller samples, which may not display the whole range of the distribution. Too large a sample, however, may obscure the actual frequency of occurrence [*Chowdhary et al*., 2011].

[33] *Genest et al*. [2009] provide a review of formal goodness-of-fit tests for copulas. Two tests, the Cramér-von Mises and Kolmogorov-Smirnov tests, were used to test the adequacy of copula models and differentiate between the suitability of each copula in capturing the dependence structure. The expressions for the Cramér-von Mises and Kolmogorov-Smirnov are, respectively, given as [*Genest et al*., 2006]

$$\begin{aligned} S_m &= \int_0^1 |\mathbb{K}_m(w)|^2 k_{\theta_m}(w)\,dw \\ &= \frac{m}{3} + m\sum_{j=1}^{m-1} K_m^2\left(\frac{j}{m}\right)\left[K_{\theta_m}\left(\frac{j+1}{m}\right) - K_{\theta_m}\left(\frac{j}{m}\right)\right] \\ &\quad - m\sum_{j=1}^{m-1} K_m\left(\frac{j}{m}\right)\left[K_{\theta_m}^2\left(\frac{j+1}{m}\right) - K_{\theta_m}^2\left(\frac{j}{m}\right)\right] \end{aligned} \tag{9}$$

and

$$T_m = \sup_{0\le w\le 1} |\mathbb{K}_m(w)| = \sqrt{m} \max_{i=0,1;0\le j\le m-1} \left\{ \left| K_m\left(\frac{j}{m}\right) - K_{\theta_m}\left(\frac{j+i}{m}\right) \right| \right\} \tag{10}$$

where $\mathbb{K}_m(w) = \sqrt{m}\{K_m(w) - K_{\theta_m}(w)\}$, $K_{\theta_m}(w) = P\{C_{\theta_m}(U, V) \le w\}$, and $k_{\theta_m}(w) = dK_{\theta_m}(w)/dw$.

[34] These tests can be employed for any type of copula. The p values associated with test statistics were computed by bootstrapping. A stepwise methodology is provided by *Genest and Favre* [2007].

5. Results and Discussions

[35] The results and discussion section is structured as follows. We first show the influence of ENSO and PDO on precipitation in each climate division and discuss the inter-decadal modulation of ENSO's impact on precipitation. We then present the choice of marginal distributions for NSOI, PDO, and precipitation and examine how the probability distribution function for precipitation changes as a result of the climate prevailing in each climate division. The copula selection procedure is presented in section 5.3. The bivariate case for average June^0–November^0 NSOI and cold season average precipitation anomaly for climate division 8 is used for illustration purposes. Finally, the results for simulation and validation of the relationship between climate indices and precipitation based on the chosen copulas are presented.

5.1. Influence of ENSO and PDO on Precipitation

[36] The influence of ENSO and PDO on both cold (October^0–March$^+$) and warm (April^0–September^0) season average monthly precipitation anomalies was examined in each of the 10 climate divisions (The notation Month^0 refers to months of the ENSO year and Month$^+$ refers to months of

the year following ENSO). October is the beginning of the hydrological year in Texas and the cold and warm seasons thus splits the water year in two 6 months periods.

[37] *Redmond and Koch* [1991] found an optimum lag of 4 months between SOI and precipitation in the western U.S. We note a statistically significant positive correlation between both average monthly June^0–November^0 NSOI and average monthly cold season PDO on the one hand, and mean monthly cold season precipitation anomalies on the other (Figure 6). The correlation between warm season indices and precipitation is negligible, consistent with previous observations [e.g., *Khedun et al*., 2012; *Kurtzman and Scanlon*, 2007; *Ropelewski and Halpert*, 1986], and will therefore not be pursued further in this study.

[38] The correlation structure for NSOI is consistently above 0.4, except for climate division 1, across the whole state. The correlation structure for PDO reveals two regions. Climate regions 1 to 4 and 8, covering the top half of the state, have a lower correlation, ranging between 0.2 (division 4) and 0.4 (division 2), while the lower southwestern half of the state has a correlation greater than 0.4. Climate division 8 has the highest correlation with NSOI (0.5) but switches to the region exhibiting lower correlation with PDO.

5.1.1. Interdecadal Modulation of ENSO's Impacts

[39] The effects of ENSO and PDO on precipitation patterns are not independent; in fact PDO modulates the effect of ENSO, leading to stronger climate responses when El Niño (La Niña) is coincident with the positive (negative) phase of PDO. When the indices are evolving in opposite phases (i.e., El Niño and negative PDO or La Niña and positive PDO), climate signals may be weaker, spatially incoherent, and unstable [*Gershunov and Barnett*, 1998].

[40] The number of times the average June^0–November^0 NSOI and average cold season PDO index were in different states were computed (Figure 8b). El Niño (La Niña) events are deemed stronger when NSOI is greater (less) than $+1$ (-1) and moderate when the index is between $+0.5$ and $+1$ (-0.5 and -1) (based on K. Redmond, Classification of El Niño and La Niña Winters, available at http://www.wrcc.dri.edu/enso/ensodef.html). For the period of record, there is a higher number of stronger El Niño than La Niña events. Also, the ratio of moderate to stronger events is 1:3, which indicates that the index rarely hovers between $+0.5$ and $+1$ or -0.5 and -1. In fact, once initiated, it eventually develops into a significant El Niño (La Niña) event. The record is split into a combined total of 54 years of stronger El Niño or La Niña, and 58 neutral years ($-1 < \text{NSOI} < 1$), implying that ENSO was either active in one of the two conditions or neutral about half the time.

[41] The average cold season PDO has an almost equal number of positive and negative cases. When the state of NSOI and PDO are considered together, an equal number of El Niño events coincident with positive PDO, and La Niña with negative PDO, are recorded. Also, the number of El Niño (La Niña) during positive (negative) PDO is higher than when they are in counter phase. Finally, more (less) El Niño (La Niña) events during negative (positive) PDO is noted.

[42] In order to verify the occurrence of positive (negative) precipitation anomalies occurring during El Niño (La Niña) events, and corresponding PDO phases, mean cold season precipitation anomalies were plotted against average June^0–November^0 NSOI (Figure 7a). Climate division 8 is chosen for illustration, as it is unique in that it has the highest correlation with NSOI and falls within the region having relatively lower correlation with PDO. The dashed lines represent the ± 1 thresholds above (below) which strong El Niño (La Niña) conditions are observed. Positive (negative) precipitation anomalies occurring during El Niño (La Niña) were identified in Figure 7a and plotted against cold season PDO (Figure 7b). It can be clearly seen that El Niño (La Niña) brings above (below) average precipitation, but there is no distinct pattern during the neutral phase of NSOI. 21% of the 112 years of data are in the El Niño-positive anomaly region and 18% are in the La Niña-negative anomaly region. When the precipitation events are

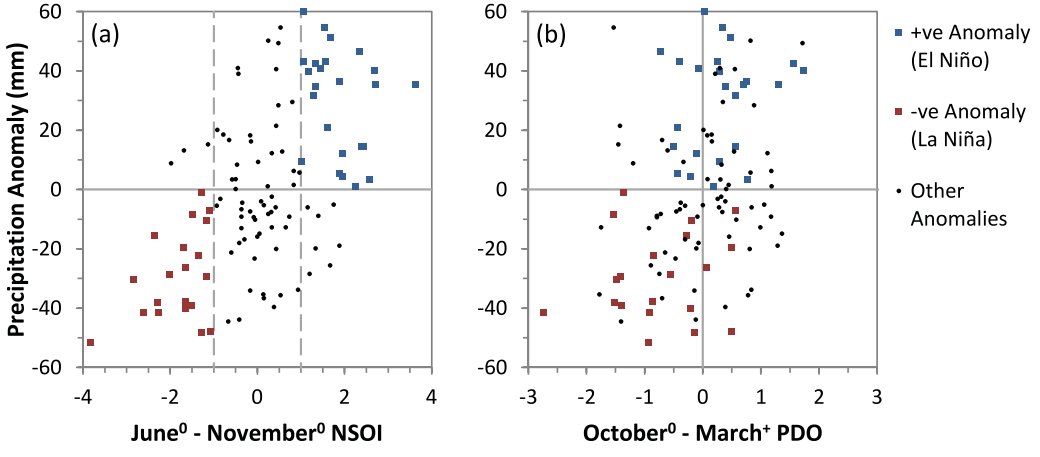

Figure 7. Scatter plot of average monthly cold season (October^0–March$^+$) precipitation anomaly versus (a) average June^0–November^0 NSOI and (b) average cold season PDO indices for climate division 8. Positive (negative) anomalies during El Niño (La Niña) events are shown in blue (red). The hit scores for blue and red events in the four quadrants of Figure 7b are $\begin{pmatrix} 8 & 16 \\ 16 & 4 \end{pmatrix}$.

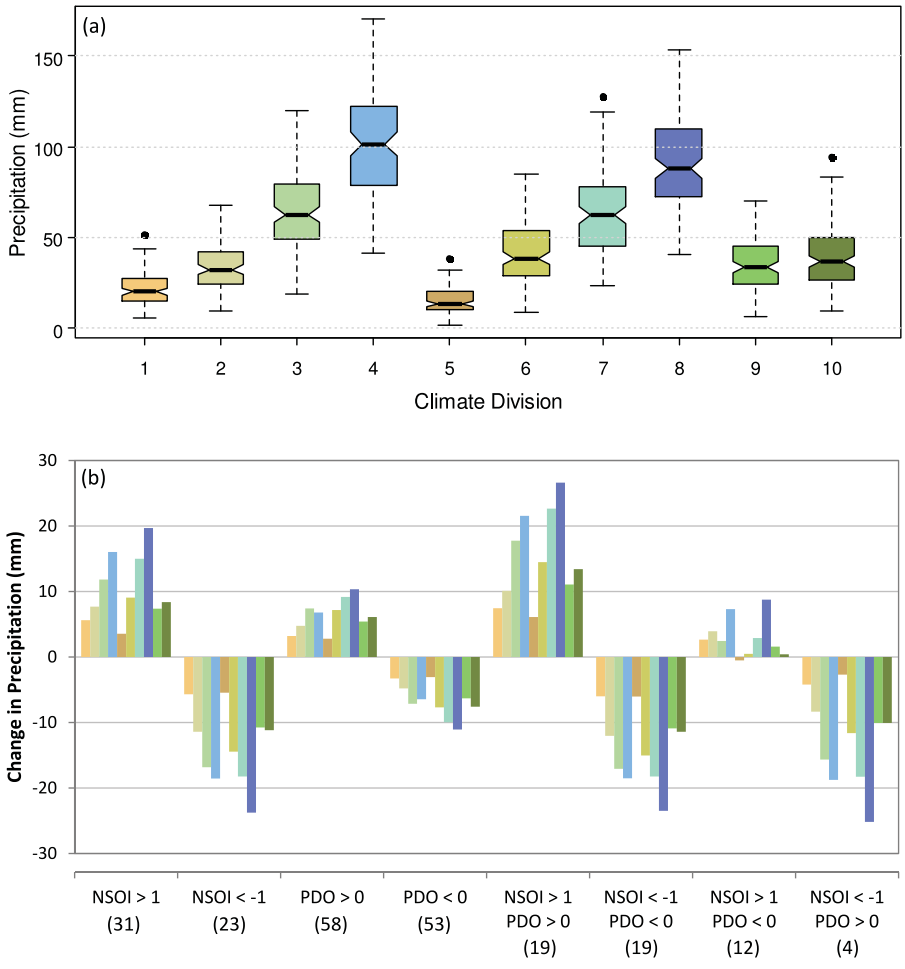

Figure 8. (a) Boxplots of average monthly cold season (October^0–March$^+$) precipitation in each climate division in Texas and (b) change in cold season (October^0–March$^+$) average precipitation for different phases of average June^0–November^0 NSOI and average cold season PDO index. Colors in Figure 8b match boxplot colors in Figure 8a. Numbers in parentheses are the number of such events in the data set.

transposed on the PDO plot, the overall precipitation pattern is no longer as distinct, which explains the lower correlation. It is nonetheless clear that there is a higher frequency of above (below) average precipitation when the indices are evolving concurrently than in opposite phases.

[43] The change in precipitation for each climate division, given different phases of NSOI and PDO, were computed and plotted along with boxplots of the average monthly cold season precipitation (Figure 8). Results confirm the hypothesized interdecadal modulation of ENSO's impacts, and also reveal that the percentage change in precipitation anomalies is not uniform across the state.

[44] In climate division 1, for example, when only El Niño events are considered, irrespective of the phase of PDO, an average increase of 5.6 mm (equivalent to 26% of the long-term mean) is noted. When only La Niña events are considered, again irrespective of the phase of PDO, the average deficit is 5.7 mm (26%). When both NSOI and PDO are positive the average increase in rainfall is 7.5 mm (34%) and when both indices are negative the average deficit is 6.0 mm (27%). Across the state, an increase ranging between 16% (division 4) and 26% (division 1) is registered during El Niño events, and a decrease ranging between 18% (division 4) and 35% (division 6) is recorded during La Niña events. A more modest increase (decrease) is noted when PDO is positive (negative). When El Niño (La Niña) occurs concurrently with positive (negative) PDO, the change in precipitation is considerably greater. El Niño events during negative PDO causes a small increase in precipitation, while La Niña events during positive PDO still result in considerable rainfall deficits, implying that irrespective of the phase of PDO, La Niña events can often have an adverse effect on water resources in the state. Spatially, the percentage change in the wetter eastern climate divisions is less than in the drier western climate divisions.

5.2. Marginal Selection

5.2.1. NSOI and PDO

[45] Marginal distribution functions for the average June^0–November^0 NSOI and the average October^0–March$^+$ PDO indices were selected from over 25

theoretical probability distributions. Based on their chi-square statistics, it was found that NSOI and PDO can be appropriately modeled by a GEV (Generalized Extreme Value) and a Weibull distribution, respectively.

[47] The maximum likelihood estimates of the parameters for the GEV and Weibull distributions are given in Table 1. Figure 9 shows the histograms for average June^0–November^0 NSOI and average October^0–March$^+$ PDO values with their respective marginal models and Q-Q plots.

5.2.2. Average Monthly Cold Season Precipitation

[48] Marginal distributions for average monthly cold season precipitation anomalies for each climate division were selected from the same suite of probability distributions used for NSOI and PDO. Table 1 gives the selected model, associated maximum likelihood estimates of its parameters, chi-square statistic, and p value for each climate division. Figure 10 is a plot of the histogram of the average cold season precipitation anomaly and selected marginal model for each climate division.

[49] It is interesting to note that the selected marginals vary with climatic conditions prevailing in each region. As evidenced by the plot of the marginal distributions, average cold season precipitation in all climate divisions, except 4, are positively skewed, with the median value being lower than the mean, implying that precipitation is generally below normal, which is typical for the southern U.S. Cold season precipitation pattern in both the western arid climate divisions 1 and 5, and eastern climate divisions 4, 8, 9, and 10, follow extreme value distributions. Western climate divisions follow shifted Weibull distributions (a.k.a. the Extreme Value Type III), while eastern climate divisions follow the GEV distribution. Note that the Weibull distribution is a special case of GEV, for which the shape parameter $\xi < 0$. The standard deviations of average cold season precipitation anomaly for climate divisions 1 and 5 ($\sigma_{1,5}$), and consequently the shape parameters of the fitted distributions, are relatively smaller compared to that of climate divisions 4 and 8, since precipitation, during the cold season, is minimal in west Texas when NAM, the major source of moisture for the region, is not active. Also, the distributions for 1 and 5 are more peaked, i.e., higher kurtosis, implying less variability in the cold season precipitation across the years.

[50] The range of average precipitation in the east is much wider, as indicated by the large standard deviation (3–4 times $\sigma_{1,5}$), and the fitted distribution becomes broader. This is due to their proximity to the Gulf of Mexico, which is a perennial source of moisture. Climate division 4, which registers the highest average cold season precipitation, is far enough north to be affected by wintertime disturbances and has enough moisture for precipitation when the disturbances arrive [*Nielsen-Gammon*, 2009]. Climate divisions 6 and 7, in the lower central part of the state, follow lognormal distribution, while climate divisions 2 and 3, in the upper central portion, follow normal and gamma distributions, respectively. The standard deviations of climate divisions 3 and 7, which are further east, are larger, and the probability of months without rainfall is relatively low, again due to the influence of the Gulf of Mexico.

Table 1. Marginal Distributions, Parameters, Chi-Square Statistics, and p Values for Average June^0–November^0 NSOI, Average Cold Season (October^0–March$^+$) PDO Index, and Average Cold Season (October^0–March$^+$) Precipitation Anomaly[a]

Variable	Distribution	Parameters	Chi-square	p Value
Climate index				
NSOI	GEV	$\hat{\xi} = -0.31$ $\hat{\sigma} = 1.38$ $\hat{\mu} = -0.32$	0.90	0.99
PDO	Weibull	$\hat{\alpha} = 5.99$ $\hat{\beta} = 4.70$ $\hat{\gamma} = -4.40$	1.81	0.94
Climate division				
1	Weibull	$\hat{\alpha} = 1.85$ $\hat{\beta} = 19.33$ $\hat{\gamma} = -17.15$	4.02	0.67
2	Normal	$\hat{\sigma} = 13.48$ $\hat{\mu} = 0.02$	2.06	0.91
3	Gamma	$\hat{\alpha} = 48.08$ $\hat{\beta} = 3.18$ $\hat{\gamma} = -152.93$	2.43	0.88
4	GEV	$\hat{\xi} = -0.31$ $\hat{\sigma} = 28.00$ $\hat{\mu} = -9.33$	3.37	0.76
5	Weibull	$\hat{\alpha} = 2.12$ $\hat{\beta} = 16.33$ $\hat{\gamma} = -14.47$	8.18	0.23
6	Lognormal	$\hat{\sigma} = 0.24$ $\hat{\mu} = 4.28$ $\hat{\gamma} = -74.07$	0.63	1.00
7	Lognormal	$\hat{\sigma} = 0.21$ $\hat{\mu} = 4.73$ $\hat{\gamma} = -115.66$	3.31	0.77
8	GEV	$\hat{\xi} = -0.18$ $\hat{\sigma} = 26.47$ $\hat{\mu} = -11.14$	4.23	0.65
9	GEV	$\hat{\xi} = -0.15$ $\hat{\sigma} = 13.17$ $\hat{\mu} = -5.90$	2.20	0.90
10	GEV	$\hat{\xi} = -0.07$ $\hat{\sigma} = 13.00$ $\hat{\mu} = -6.64$	0.61	1.00

[a]Gamma: $f(x) = \frac{(x-\gamma)^{\alpha-1}}{\beta^{\alpha}\Gamma(\alpha)} \exp(-(x-\gamma)/\beta)$ where α, β, γ and are the shape, scale, and location parameters, respectively. GEV: $f(x) = \begin{cases} \frac{1}{\sigma}\exp(-(1+\xi z)^{-1/\xi})(1+\xi z)^{-1-1/\xi}, \xi \neq 0 \\ \frac{1}{\sigma}\exp(-z-\exp(-z)), \xi = 0 \end{cases}$, where $z \equiv \frac{x-\mu}{\sigma}$, and ξ, σ, and μ are the shape, scale, and location parameters, respectively. Lognormal: $f(x) = \frac{\exp\left(-\frac{1}{2}\left(\frac{\ln(x-\gamma)-\mu}{\sigma}\right)^2\right)}{(x-\gamma)\sigma\sqrt{2\pi}}$, where σ, μ, and γ are the shape, scale, and location parameters, respectively. Normal: $f(x) = \frac{\exp\left(-\frac{1}{2}\left(\frac{x-\mu}{\sigma}\right)^2\right)}{\sigma\sqrt{2\pi}}$ where σ and μ are the scale and location parameters, respectively. Weibull: $f(x) = \frac{\alpha}{\beta}\left(\frac{x-\gamma}{\beta}\right)^{\alpha-1}\exp\left(-\left(\frac{x-\gamma}{\beta}\right)^{\alpha}\right)$ where α, β, and γ are the shape, scale, and location parameters, respectively.

5.3. Copula Selection

5.3.1. Copula Parameter Estimation

[51] Precipitation anomalies exhibit a positive association between NSOI (and PDO) in Texas (Figure 6). Note that SOI was converted to NSOI to ensure positive association and thus reduce the number of potential copulas. For climate division 8, the sample estimates of the Pearson correlation coefficient, Kendall's tau, and Spearman's rho are 0.54, 0.35, and 0.51, respectively, with corresponding p values of 1.22e-09, 3.44e-08, and 8.89e-09.

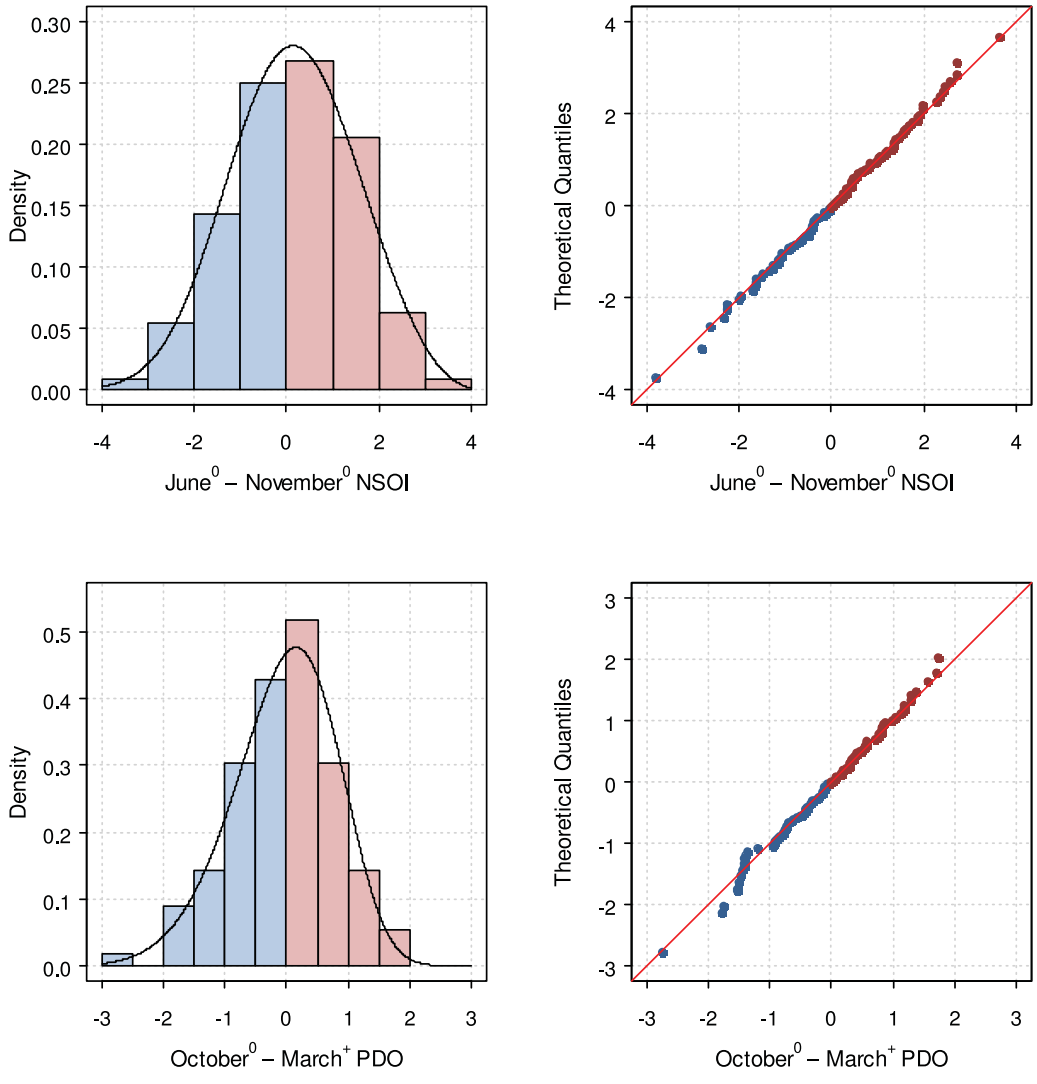

Figure 9. Histograms and Q-Q plots of average June^0–November^0 NSOI and average October^0–March$^+$ PDO index. NSOI follows GEV and PDO follows Weibull. Negative (positive) values are shown in blue (red).

The association between the two variables was further explored graphically through Kendall's plot (K-plot) and chi-plots (Figure 11). A K-plot is equivalent to a Q-Q plot, but where data points falling on $y=x$ diagonal indicate that u_1 and u_2 are independent and points above (below) the diagonal line indicate positive (negative) dependence. Chi-plots [*Fisher and Switzer*, 2001] are based on the chi-square statistics for independence in a two-way table [*Genest and Favre*, 2007] and λ_i is a measure of the distance of the points $(u_{1,i},\ u_{2,i})$ from the center of the data, defined by its median $(\tilde{u}_1,\ \tilde{u}_2)$. In case of no relationship between the two variables, 95% of the data points should fall within the two control lines. Both the K- and chi-plots suggest significant positive dependence. Further, the chi-plots for the lower and upper tails (where lower (upper) tail is defined for those $u_{1,i}$ and $u_{2,i}$ values that are smaller (larger) than their respective means), suggest that the data exhibit both lower and upper tail dependence. Moreover, stronger lower than upper tail dependence is also visible from the plots, which implies that the influence of ENSO during La Niña is more apparent than during El Niño.

[52] Based on information garnered from the correlation coefficients and graphically illustrated dependence structure, sets of one- and two-parameter copulas were chosen as potential candidates for modeling the relationship between average June^0–November^0 NSOI and average cold season precipitation anomalies. The generating function, parameter space, relationship of nonparametric dependence measure, and lower and upper tail dependence for the bivariate form of each copula are given in Table 2 [*Schepsmeier and Brechmann*, 2013].

[53] The dependence parameter(s) for each copula was (were) determined using the maximum pseudo-likelihood method, which ensures that the dependent structure is determined independently of the margins. The corresponding Kendall's tau values, maximized log-likelihood values ($LL_{\max}$) and Akaike and Bayesian Information Criteria (expressions for AIC and BIC, respectively, are given as footnotes to Table 3) were also computed.

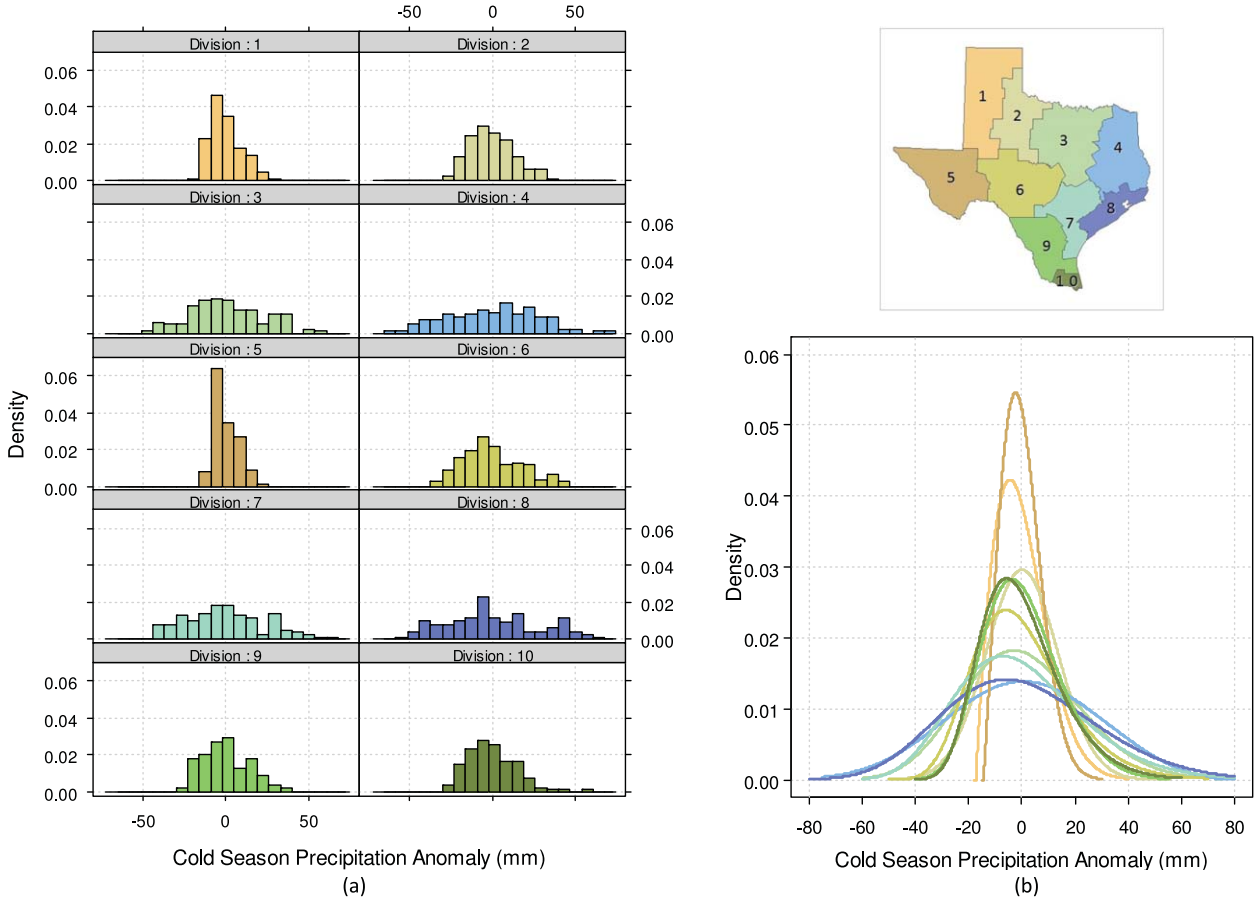

Figure 10. (a) Histogram of average cold season (October^0–March$^+$) precipitation anomaly and (b) plot of selected marginal distribution for each climate division.

5.3.2. Goodness-of-Fit Tests

[54] For each copula considered, two formal goodness-of-fit tests were performed: Cramér-von Mises and Kolmogorov-Smirnov. Table 3 gives the test statistics and associated p values, computed using bootstrapping based on random samples of size 1000, except for the Gaussian copulas, where computational constraints limited the sample size to 100. Four copulas (Gumbel, Frank, BB 6, and BB 8) can be rejected as viable models at 5% significance level. Based on AIC and BIC, the Gaussian, Student's t, and Clayton copulas appear to be most suited to model the dependence structure between average June^0–November^0 NSOI and average cold season precipitation anomaly in climate division 8. Note that since for large degrees of freedom, the Student's t copula tends to a Gaussian copula, only the latter and Clayton copulas will be analyzed further.

[55] Figure 12 allows a visual comparison of the observed data with random samples generated from the Gaussian and Clayton copulas. Positive (negative) precipitation anomalies occurring during El Niño (La Niña) are identified as in Figure 7a. Note that the extreme lower left data point is associated with the 1917 drought, where the average June^0–November^0 NSOI was −3.82 and associated average cold season precipitation anomaly was −51.59 mm, i.e., coordinates (−3.82, −51.59). By contrast, the recent 2011 drought has coordinates (−2.62, −41.43).

[56] The spread of the two copulas are visibly different; even though they both envelop the observed data, they exhibit different tail behaviors. Lower and upper tail dependence in the Gaussian copula is weak, whereas the Clayton copula exhibits strong lower tail and weak upper tail dependence. The relationship between average June^0–November^0 NSOI and average cold season precipitation anomaly does exhibit some degree of lower tail dependence, especially when the major drought events are considered (1917 (−3.82, −51.59), 1950 (−2.28, −38.04), 1975 (−2.83, −30.42), and 2011 (−2.62, −41.43)), a feature which, graphically, makes Clayton a more attractive copula. However, based on analytical goodness-of-fit results, the Gaussian copula is deemed most suited for this climate division.

5.3.3. NSOI and Precipitation Anomaly

[57] Following the steps illustrated in sections 5.3.1 and 5.3.2, copulas were fitted to all 10 climate divisions in the state. Table 4 gives the most suited copula and associated parameter and goodness-of-fit statistics for each climate division.

[58] Most copulas exhibit similar forms in their central part but differ significantly in the tails, where extreme values are located. Given that each climate division is subject to different climatologic conditions and subject to a number of small- and large-scale meteorological regimes, the degree of dependence with NSOI varies, hence the

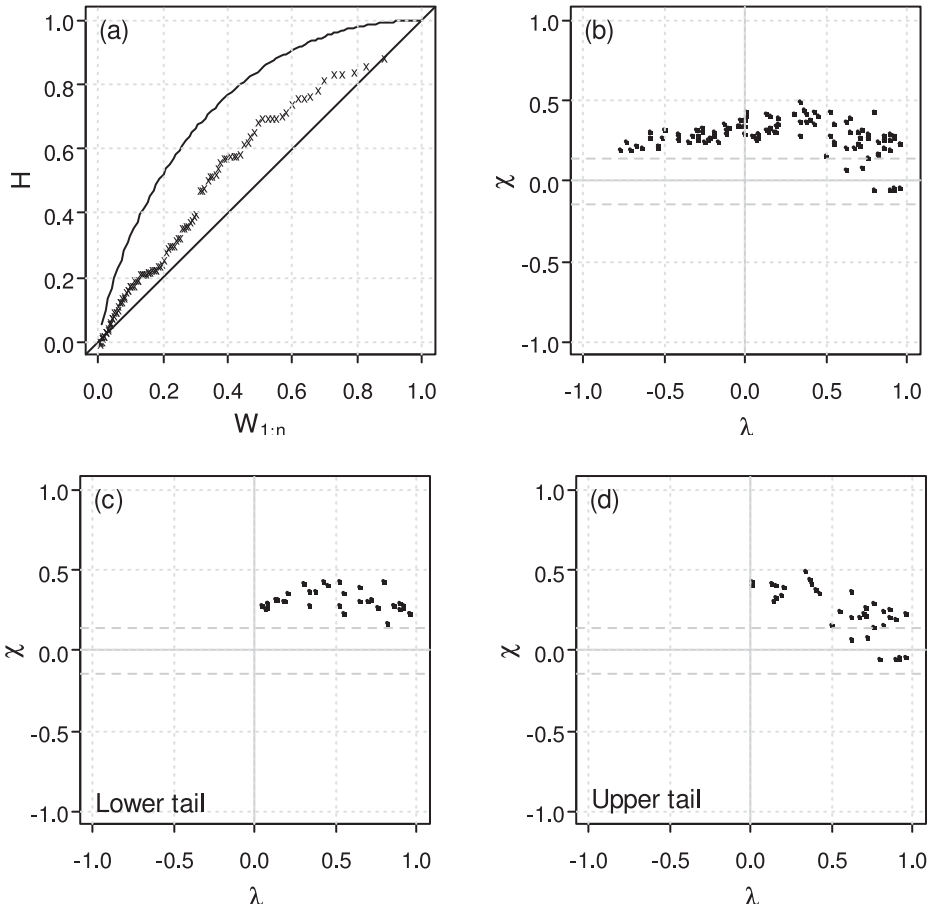

Figure 11. Dependence between average June^0–November^0 NSOI and average cold season precipitation anomaly for climate division 8 illustrated through (a) Kendall's plot and (b–d) chi-plots.

difference in the selected copula. It is important to note that since the maximum pseudo-likelihood method was used for the copula selection, the chosen copula is independent of the marginals and solely due to the dependence structure.

[59] Cold season precipitation in the western part of the state, as shown in section 5.2.2, is minimal and not highly variable given the limited sources of moisture. Further, the correlation of average cold season precipitation with average June^0–November^0 NSOI is relatively small. The most suited copula for modeling the dependence in climate divisions 1 and 5 are Gaussian and Frank, respectively. The difference between the Gaussian and Frank copulas is in the intermediate area, where the Frank copula exhibits a stronger dependence, but at the tails, the Gaussian copula tends to be stronger. The Gaussian copula is also the most suitable copula for climate divisions 4, 8, and 10, which are located on the wettest part of the state. Despite strong correlation between NSOI and precipitation for these climate divisions, there is no distinct tail dependence, which leads us to infer that other meteorological effects, most likely a result of their proximity to the Gulf of Mexico, may tend to mask drought events that may be due to La Niña.

[60] The copula deemed suitable for modeling the dependence between NSOI and precipitation in climate divisions 2, 3, 6, 7, and 9, located in the central part of the state, is Clayton. Clayton's $\theta \to 0$ indicates that the marginals are independent, and as $\theta \to \infty$, the copula attains the Fréchet upper bound. It does not, however, attain the Fréchet lower bound. The Clayton copula exhibits a strong lower tail dependence, but a relatively weak upper tail dependence, which implies that there is a strong association between negative NSOI (La Niña) and precipitation conditions, while the association between positive NSOI (El Niño) may be either weaker or obscured by local meteorological conditions.

[61] Finally, it is surprising to note that two-parameter copulas, considered in this study because of their ability in capturing more than one type of dependence, were not selected in any of the 10 climate divisions. However, they do rank as the second best choice in some climate divisions (e.g., divisions 4 and 10).

5.3.4. PDO and Precipitation Anomaly

[62] The same set of copulas considered for NSOI and precipitation anomaly were considered to model the dependence structure between average cold season PDO and average October^0–March$^+$ precipitation anomaly. The Gaussian copula dominates the dependence structure between PDO and precipitation across the state. Note that due to the relatively high variability in precipitation, attributed partly to the influence of ENSO and partly to local meteorological factors, the correlation between PDO and precipitation is lower than with NSOI. Further, PDO has a long cycle of about 20 to 30 years and hence its influence can be qualified as more subtle, which explains the absence

Table 2. Generating Function, Parameter Space, Relationship of Nonparametric Dependence Measure With Association Parameter, and Lower and Upper Tail Dependence for the Bivariate Form of Each of the 10 Copulas Used in This Study

Copula	Generator	Parameter Space	Kendall's τ	Tail Dependence	
				Lower (λ_L)	Upper (λ_U)
Elliptical Copula					
Gaussian		$\rho \in (-1,1)$	$\frac{2}{\pi}\arcsin(\rho)$	0	0
Student's t		$\rho \in (-1,1), \nu > 2$	$\frac{2}{\pi}\arcsin(\rho)$	$2t_{\nu+1}\left(-\sqrt{\nu+1}\sqrt{\frac{1-\rho}{1+\rho}}\right)$	
Archimedean Copula					
Clayton	$\frac{1}{\theta}(t^{-\theta}-1)$	$\theta > 0$	$\frac{\theta}{\theta+2}$	$2^{-1/\theta}$	0
Gumbel	$(-\log t)^{\theta}$	$\theta \geq 1$	$1-\frac{1}{\theta}$	0	$2-2^{1/\theta}$
Frank[a]	$-\log\left[\frac{e^{-\theta t}-1}{e^{-\theta}-1}\right]$	$\theta \in \mathbb{R}\setminus\{0\}$	$1-\frac{4}{\theta}+4\frac{D_1(\theta)}{\theta}$	0	0
Joe	$-\log[1-(1-t)^{\theta}]$	$\theta > 1$	$1+\frac{4}{\theta^2}\int_0^1 t\log(t)(1-t)^{\frac{2(1-\theta)}{\theta}}dt$	0	$2-2^{1/\theta}$
BB 1	$(t^{-\theta}-1)^{\delta}$	$\theta > 0, \delta \geq 1$	$1-\frac{2}{\delta(\theta+2)}$	$2^{-1/(\theta\delta)}$	$2-2^{1/\delta}$
BB 6	$(-\log[1-(1-t)^{\theta}])^{\delta}$	$\theta \geq 1, \delta \geq 1$	$1+\frac{4}{\delta\theta}\int_0^1(-\log(1-(1-t)^{\theta})\times(1-t)(1-(1-t)^{-\theta}))dt$	0	$2-2^{1/(\theta\delta)}$
BB7[b]	$[1-(1-t)^{\theta}]^{-\delta}-1$	$\theta \geq 1, \delta > 0$	$1-\frac{2}{\delta(2-\theta)}+\frac{4}{\theta^2\delta}B\left(\frac{2-\theta}{\theta},\delta+2\right)$	$2^{-1/\delta}$	$2-2^{1/\theta}$
BB 8	$-\log\left[\frac{1-(1-\delta t)^{\theta}}{1-(1-\delta)^{\theta}}\right]$	$\theta \geq 1, \delta \in (0,1]$	$1+\frac{4}{\delta\theta}\int_0^1\left(-\log\left(\frac{(1-t\delta)^{\theta}-1}{(1-\delta)^{\theta}-1}\right)\times(1-t\delta)(1-(1-t\delta)^{-\theta})\right)dt$	0	0^{c}

[a] $D_1(\theta)=\int_0^{\theta}\frac{c/\theta}{exp(x)-1}dx$ (Debye function).

[b] $B(x,y)=\int_0^1 t^{x+1}(t-1)^{y-1}dt$ (Beta function).

[c] $2-2^{1/\theta}$ if $\delta=1$, otherwise 0.

of strong tail dependence (both upper and lower) and the choice of Gaussian as the most appropriate copula.

5.3.5. NSOI, PDO, and Precipitation Anomaly

[63] Three climate divisions were chosen for further analysis, simulation, and prediction of average cold season precipitation anomalies, using the state of NSOI and PDO as precursors: 5 located in the arid west; 7 straddling two different climate regions in the middle-eastern part; and 8 representing the wettest region in the state.

[64] In this section, the most appropriate copula for modeling the dependence between both large-scale circulation patterns (average June^0–November^0 NSOI and average

Table 3. Parameter(s), Kendall's Tau, Maximum Log-Likelihood, AIC, BIC, and Cramér-von Mises and Kolmogorov-Smirnov Goodness-of-Fit Statistics, Along With Their Respective p Values, for Each Copula for Climate Division 8[a]

Copula	$\hat{\rho}$ or $\hat{\theta}$	$\hat{\delta}$	τ	$LL_{\max}$	AIC[a]	BIC[a]	S_n Statistic	S_n p	T_n Statistic	T_n p
Gaussian	0.55		0.37	18.55	−35.09	−32.37	0.10	0.23	0.67	0.50
Student's t	0.54		0.37	18.05	−34.09	−31.37	0.08	0.37	0.61	0.58
Clayton	0.92		0.32	17.81	−33.62	−30.90	0.12	0.19	0.85	0.21
Gumbel	1.44		0.31	12.60	−23.19	−20.47	0.22	0.01	1.03	0.03
Frank	3.51		0.35	16.33	−30.66	−27.94	0.14	0.05	0.73	0.26
Joe	1.51		0.22	7.59	−13.17	−10.45	0.71	0.98	1.70	0.93
BB 1	0.75	1.09	0.34	18.04	−32.08	−26.65	0.10	0.26	0.73	0.37
BB 6	1.00	1.44	0.31	12.59	−21.18	−15.74	0.22	0.02	1.03	0.04
BB7	1.06	0.90	0.32	17.84	−31.68	−26.24	0.11	0.19	0.81	0.24
BB 8	6.00	0.46	0.33	15.47	−26.93	−21.49	0.18	0.02	0.89	0.09

[a] τ = Kendall's tau; $LL_{\max}$ = maximum log-likelihood; S_n statistic = Cramér-von Mises statistics; S_n p = p value for Cramér-von Mises goodness-of-fit test; T_n statistic = Kolmogorov-Smirnov statistics; T_n p = p value for Kolmogorov-Smirnov goodness-of-fit test.

$$AIC=-2\sum_{i=1}^{N}\ln[c(u,v|\boldsymbol{\theta},\boldsymbol{\delta})]+2k.$$

$$BIC=-2\sum_{i=1}^{N}\ln[c(u,v|\boldsymbol{\theta},\boldsymbol{\delta})]+ln(N)k$$ where N is the length of the observations and k is the number of copula parameters.

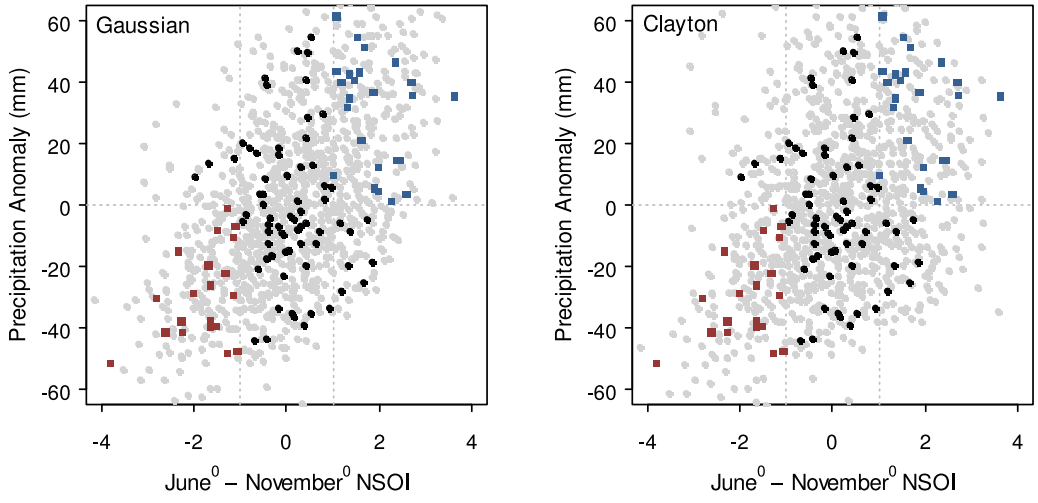

Figure 12. Comparison of observed data with 1000 random samples generated from the Gaussian and Clayton copula (solid light gray dots) for climate division 8. Observed positive (negative) anomalies during El Niño (La Niña) events are shown in blue (red) and other events are shown in solid black dots (similar to Figure 7a).

cold season PDO) and average cold season precipitation anomaly is discussed. From the results of the bivariate analysis, three copulas (Clayton, Frank, and Gaussian) were shortlisted for modeling the predictor and dependent variables. The parameter estimates, maximum log-likelihood, goodness-of-fit statistic, and p value for each, are given in Table 5. The Clayton copula does not fare well (very low p values) in all three climate divisions, implying that there is no distinct lower tail dependence anymore. Based on the maximum log-likelihood values, which is equivalent to comparing AIC since all three copulas are single parameter, the Gaussian copula seems most suitable for modeling the three variables. Given that the Gaussian copula is deemed better than the Frank copula indicates that there is some dependence at the tails.

5.4. Simulation

[65] For the three climate divisions (5, 7, and 8), representing three varying climate regimes and dependence with NSOI and PDO, random values were generated from the chosen copula to assess how the model simulates the precipitation for different cases or ranges of NSOI and PDO. The bivariate case, between NSOI and precipitation anomaly is first considered, and the influence of PDO, in a trivariate model, is then discussed.

[66] *Embrechts et al*. [2003] provide an effective algorithm for the generation of random variates for an m-variate distribution, such that $U_1, \ldots, U_m$ have joint distribution

Table 4. Parameter and Cramér-von Mises and Kolmogorov-Smirnov Goodness-of-Fit Statistics, Along With Their Respective p Values, for the Copula Selected for Modeling the Dependence Between Average June^0–November^0 NSOI and Average Cold Season Precipitation Anomaly for Each Climate Division

Climate Division	Copula	$\hat{\rho}$ or $\hat{\theta}$	S_n Statistic	S_n p	T_n Statistic	T_n p
1	Gaussian	0.40	0.06	0.80	0.57	0.86
2	Clayton	0.81	0.05	0.76	0.63	0.71
3	Clayton	0.78	0.05	0.74	0.56	0.85
4	Gaussian	0.46	0.06	0.64	0.76	0.35
5	Frank	2.73	0.06	0.59	0.63	0.58
6	Clayton	0.81	0.07	0.61	0.77	0.35
7	Clayton	0.92	0.08	0.42	0.76	0.38
8	Gaussian	0.55	0.10	0.23	0.67	0.50
9	Clayton	0.82	0.16	0.06	0.91	0.11
10	Gaussian	0.53	0.06	0.53	0.59	0.72

Table 5. Parameter(s), Maximum Log-Likelihood, and Cramér-von Mises Goodness-of-Fit Statistics Along With Its p Values, for the Clayton, Frank, and Gaussian Copulas Modeling the Dependence Between Average June^0–November^0 NSOI, Average Cold Season PDO, and Average Cold Season Precipitation Anomaly for Climate Divisions 5, 7, and 8

Climate Division	5	7	8
Clayton copula			
Parameter (std. error)	0.60 (0.10)	0.71 (0.13)	0.68 (0.11)
Maximum log-likelihood	24.18	30.71	28.62
S_n statistic	0.09	0.07	0.08
S_n p	0.00	0.04	0.02
Frank copula			
Parameter	2.71 (0.426)	2.85 (0.44)	2.77 (0.41)
Maximum log-likelihood	26.03	27.33	26.26
S_n statistic	0.05	0.05	0.05
S_n p	0.11	0.15	0.05
Gaussian copula[a]			
ρ_1	0.49 (0.08)	0.49 (0.08)	0.49 (0.08)
ρ_2	0.44 (0.08)	0.52 (0.07)	0.55 (0.08)
ρ_3	0.45 (0.07)	0.44 (0.09)	0.36 (0.07)
Maximum log-likelihood	28.92	32.58	32.99
S_n statistic	0.03	0.03	0.03
S_n p	0.36	0.37	0.26

[a]Position of ρs in an unstructured Gaussian matrix

$$\begin{array}{c} \\ NSOI \\ PDO \\ Pcp \end{array} \begin{array}{c} \begin{array}{ccc} NSOI & PDO & Pcp \end{array} \\ \begin{pmatrix} 1 & \rho_1 & \rho_2 \\ \rho_1 & 1 & \rho_3 \\ \rho_2 & \rho_3 & 1 \end{pmatrix} \end{array}$$

function C. For k-dimensional margins of C, let $C_k(u_1, \ldots, u_k) = C(u_1, \ldots, u_k, 1, \ldots, 1)$ with $k = 2, \ldots, m-1$, and $C_1(u_1) = u_1$ and $C_m(u_1, \ldots, u_m) = C(u_1, \ldots, u_m)$. The conditional distribution of U_k given $U_1, \ldots, U_{k-1}$, is given by

$$C_k(u_k|u_1, \ldots, u_{k-1}) = \mathbb{P}\{U_k \leq u_k | U_1 = u_1, \ldots, U_{k-1} = u_{k-1}\} = \frac{\partial^{k-1} C_k(u_1, \ldots, u_k)}{\partial u_1 \ldots \partial u_{k-1}} \Big/ \frac{\partial^{k-1} C_{k-1}(u_1, \ldots, u_{k-1})}{\partial u_1 \ldots \partial u_{k-1}} \tag{11}$$

assuming that both numerator and denominator exist and the denominator is not zero. This algorithm can be used to simulate the whole range of the joint distribution, or for the prediction of the range of response variables given an explanatory value.

5.4.1. Bivariate Simulation: NSOI and Precipitation Anomaly

[67] Figure 13 shows boxplots of both observed values and that simulated from the selected copula for different NSOI ranges for climate divisions 5, 7, and 8. Notched boxplots are preferred as they visually depict the significance between the observed values and simulated data. Nonoverlapping notches indicate that the medians are significantly different at a 95% confidence level. The size of the notch around each median (M) is calculated as $M \pm Cs$, where C is a constant chosen to be 1.7 and $s = 1.25R/1.35\sqrt{N}$ is the Gaussian-based asymptotic approximate of the standard deviation of the median with R being the interquartile range and N the number of observations in each group [*McGill et al.*, 1978].

[68] When the whole range of NSOI is considered ($-4 < \mathrm{NSOI} < 4$), the interquartile ranges of both the observed and simulated data overlap and the medians are not significantly different. The medians in all cases are lower than the means, indicating a higher probability of precipitation deficit, which is typical for the state. The skewness and kurtosis of the simulated values agree fairly well with the observations. When specific ranges of NSOI are considered, we note that there is better agreement between observed and simulated values when NSOI < -1 than when NSOI > 1. Better simulation of values in the lower left quadrant is expected given that lower tail dependence is stronger in the observed data (Figure 11).

5.4.2. Trivariate Simulation: NSOI, PDO, and Precipitation Anomaly

[69] Figure 14 shows the boxplots of observed and simulated values for different NSOI and PDO ranges for climate divisions 5, 7, and 8. When the whole range of NSOI is considered, irrespective of the state of PDO, the interquartile ranges of both the observed and simulated data overlap and the medians are not significantly different. The basic statistics of observed and simulated data agree fairly well on the whole. When the data is stratified into cases when PDO is negative and positive, depicted with a light blue and light red background, respectively, an interesting trend emerges. Inclusion of PDO in the model generally improves the simulation results, especially for the cases when PDO is negative. Better agreement between observed and simulated values is noted in the lower left quadrant, that is negative precipitation anomaly due to La Niña and negative PDO, but no significant improvement can be seen in the upper right quadrant (positive precipitation anomaly during El Niño coincident with positive PDO).

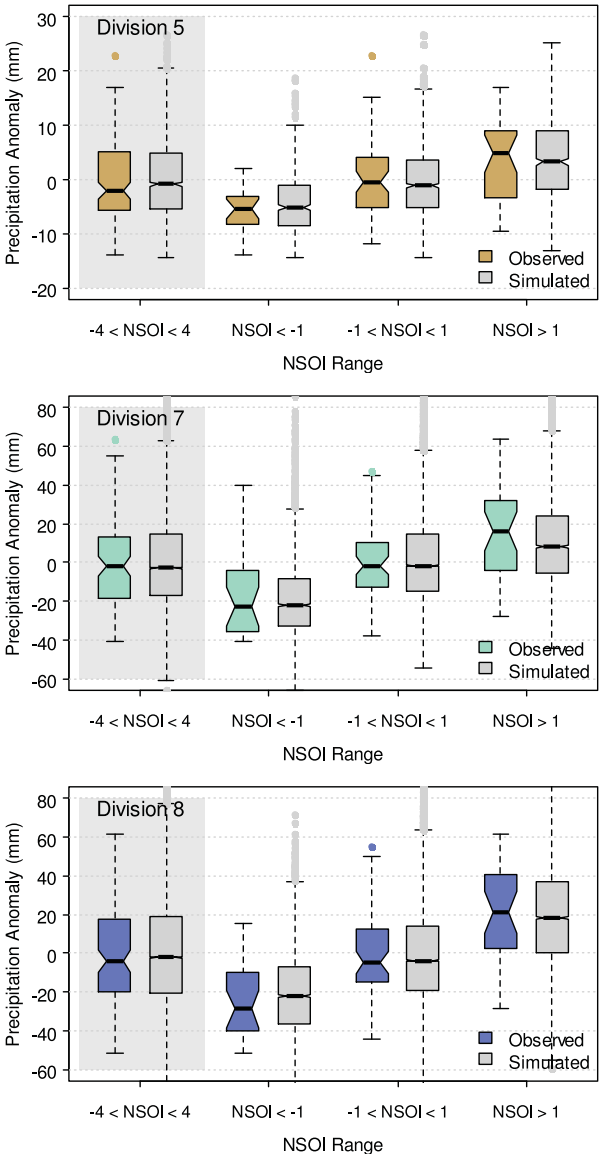

Figure 13. Boxplots of observed and simulated cold season precipitation anomalies for different NSOI ranges for climate divisions 5, 7, and 8. Boxplots with light gray background are for complete NSOI range.

[70] In climate division 8, for example, the absolute difference between the means of observed and simulated values for NSOI < -1 in the bivariate model is 6.1 mm. In the trivariate model, the absolute difference between the observed and simulated means for NSOI < -1 and negative PDO is only 0.8 mm. The absolute difference in medians for the bivariate model is 7.4 mm while that for the trivariate model is 4.6 mm (Table 6). Improvements are also noted in the lower and upper quartiles (absolute difference of 7.2 mm and 2.3 mm, respectively, in the bivariate model reduced to 0.2 and 1.3 mm, respectively, in the trivariate model). Similar improvements, albeit of different magnitude, given that the monthly rainfall is lower, were seen in climate divisions 5 and 7. In climate division 7, however,

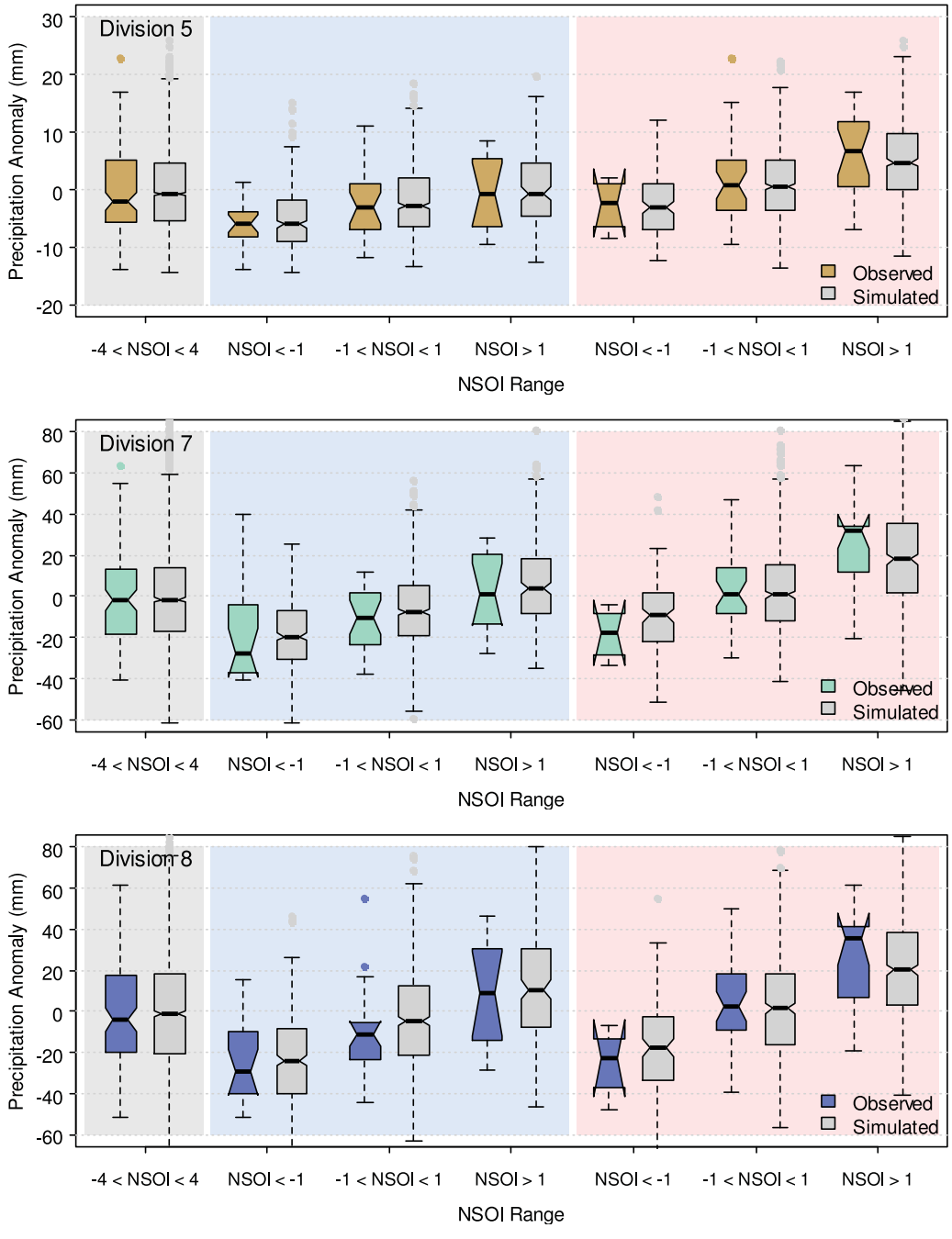

Figure 14. Boxplots of observed and simulated cold season precipitation anomalies for different NSOI and PDO ranges for climate divisions 5, 7, and 8. Boxplots with light gray background are for complete NSOI and PDO ranges and light blue (red) is for different NSOI ranges and negative (positive) PDO.

the median did not improve even though the mean improved. One possible reason for this discrepancy can be due to the fact that climate division 7 is not homogenous as it straddles two different climate regions (Figure 1) and the lower half is exposed to oceanic influences. Comparable discrepancies in behavior for stations lying at the intersection of climate regions in Texas were noted by *Mishra et al*. [2011].

[71] These results highlight the importance of including PDO in the probabilistic prediction of precipitation. While ENSO, being a strong large-scale circulation pattern modulating climatic conditions over the whole planet, is an important determinant of precipitation conditions, it does not fully explain the variability between El Niño (La Niña) events [*Khedun et al*., 2012]. Knowledge of the state of PDO can greatly improve our expectation of precipitation conditions. La Niña coincident with negative PDO have been shown to increase drought severities, while positive PDO may lead to above average precipitation, despite negative ENSO conditions [*Cole et al*., 2002]. The trivariate copula model does fairly well in simulating conditions when PDO is negative, but not as well when PDO is

Table 6. Comparison of Means and Medians for Observed and Simulated Cold Season Precipitation Anomalies From the Bivariate and Trivariate Models for Climate Divisions 5, 7, and 8

	Bivariate Model			Trivariate Model		
	NSOI < -1			NSOI < -1 and PDO < 0		
NSOI and PDO Range	Observed	Simulated	Absolute Difference	Observed	Simulated	Absolute Difference
Division 5						
Mean	−5.44	−3.78	1.66	−6.02	−4.76	1.26
Median	−5.40	−4.77	0.63	−5.86	−5.92	0.06
Division 7						
Mean	−18.23	−17.71	0.52	−18.23	−18.56	0.33
Median	−22.69	−21.26	1.43	−27.40	−21.04	6.35
Division 8						
Mean	−23.76	−17.71	6.05	−23.466	−22.69	0.77
Median	−28.69	−21.26	7.43	−29.490	−24.93	4.56

positive, especially when both NSOI and PDO are positive. This is due to the limitation of this simplistic model in simulating the complex local and remote drivers of precipitation [*Westra and Sharma*, 2010]. A possible explanation is that during a drought, once dry conditions are initiated, the ground loses soil moisture, which can further intensify local conditions by raising the ground temperature and creating a high pressure system, which may suppress rainfall. On the other hand, even low rainfall event can increase soil moisture, which evaporates back and increases humidity level in the atmosphere along with evaporation from surface waters in lakes and rivers, and in this case moisture from the Gulf of Mexico. When temperature and other meteorological conditions are conducive, this leads to more precipitation. These local conditions may not be influenced by large-scale climate phenomena, hence the high variability in the upper right quadrant of the data set, which the copula model is unable to capture; hence the lower mean and median in the simulated values as opposed to the observed data.

5.5. Precipitation Prediction Using Copula Models

[72] In this section, we present how the copula models discussed in the previous sections can be used for predicting precipitation anomalies given the state of NSOI and PDO. The prediction capabilities of the bivariate case, that is NSOI and precipitation anomaly, is compared against the trivariate model, which incorporates PDO, for climate divisions 5, 7, and 8. They experience very different climate regimes and the average cold season precipitation anomalies follows different marginal distributions.

[73] The 112 year long data set was divided into two sets; one for constructing the model and the other for validation. The modeling set contained 70% of the data and the remaining 30% was used for validation. The following procedure was adopted for the selection of the validation data set. The average June^0–November^0 NSOI, average cold season PDO, and average cold season precipitation anomalies (for all three climate divisions) matrix was stratified based on NSOI values followed by PDO values, and representative samples were randomly selected from each stratum. This procedure ensures that the overall dependence structure is not impaired while enough data points are obtained in each case. Thus, the models remain unbiased, as it would be when the whole data set is used for cold season precipitation forecasting. Further, extracting the validation data once, and not repeating the procedure separately for each climate division, allows comparison of the model performance across different climate conditions.

[74] Copulas were fitted to the modeling data, from the same set of copulas considered above and following the same procedure described in section 5.3. Again, note that the maximum pseudo-likelihood method was used, which ensures that the copula selected is independent of the marginals and due to the dependence structure only. Despite our attempt to preserve the overall dependence structure in the modeling data set, the copulas chosen for the bivariate models were different, except for climate division 7, from those selected when the whole data set were used. Clayton, with different $\hat{\theta}$ parameters, was deemed the most suitable copula for all three cases. However, for the trivariate models, Gaussian again emerged as the most suitable copula for modeling NSOI, PDO, and precipitation anomaly.

[75] Once the most appropriate copula was selected, the response variable, conditioned upon the explanatory variable(s), was obtained using equation (11). The results were in the unit hypercube domain and were back transformed, using the fitted marginals, to obtain the average cold season precipitation anomalies.

[76] The predicted values against observed values for the bivariate and trivariate case, for all three climate divisions, are shown as scatterplots in Figure 15. The coefficient of correlation between the predicted and observed values for the bivariate case is 0.66, 0.69, and 0.60 for climate divisions 5, 7, and 8, respectively. When PDO is included, the correlation drops slightly to 0.58, 0.60, and 0.42. This drop in correlation is expected given the high variability in precipitation due to local meteorological conditions, as illustrated with simulations, especially when both NSOI and PDO are positive. Interestingly, however, the correlation between observed and predicted values in the lower left quadrant, that is, when both NSOI and PDO are negative, is significantly improved in the trivariate model. Correlation of values within that quadrant increased from 0.26, 0.45, and 0.35 (bivariate case) to 0.65, 0.53, and 0.71 for climate divisions 5, 7, and 8, respectively. This result is in accord with the improved simulation ranges observed when PDO was negative.

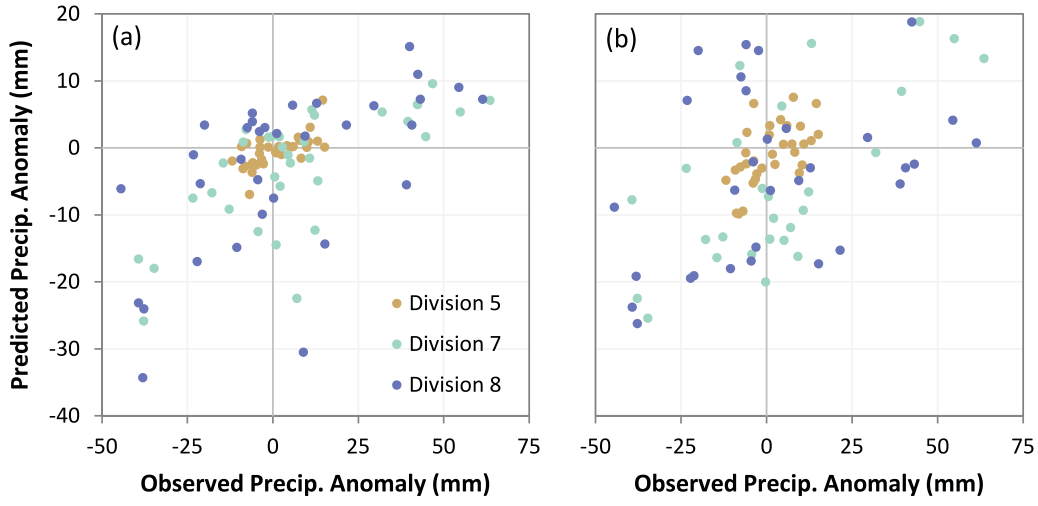

Figure 15. Scatter plot of predicted versus observed average cold season rainfall anomaly for (a) NSOI and precipitation anomaly models and (b) NSOI, PDO, and precipitation anomaly models.

6. Conclusions

[77] Precipitation in the state of Texas is influenced by large-scale circulation patterns in the Pacific Ocean. A statistically significant correlation between both average June^0–November^0 NSOI, and average cold season (October^0–March$^+$) PDO, with average cold season precipitation was found. The spatial correlation patterns for the two indices, across the 10 different climate divisions in the state, are not identical. Higher correlation with NSOI was recorded than with PDO. Nonetheless, the effect of PDO can be significant.

[78] PDO has been known to modulate the effect of ENSO, leading to stronger response when they are coincident, particularly when they are negative, than when they are out of phase. In this study, a copula-based model was developed to assess how well ENSO conditions alone can predict precipitation and if including the state of PDO improves the prediction. Copulas were used to model the bivariate dependence between NSOI and precipitation anomaly and the trivariate dependence between NSOI, PDO, and precipitation anomaly. Ten copulas, from the elliptical and Archimedean families, were evaluated. Three of the copulas considered were two-parameter copulas, as they can capture more than one type of dependence. The copulas were fitted using the maximum pseudo-likelihood method which ensures that the selected copula is independent of the marginals. Different copulas were found to be suitable for different climate divisions. The choice of copula is strongly driven by the lower tail dependence which is associated with La Niña conditions and negative precipitation anomaly.

[79] Using the chosen copula, precipitation was simulated from the bivariate and trivariate models for three different climate divisions: 5, which is semi-arid; 8, located in the wettest region; and 7 in the middle-eastern region, straddling the subtropical humid and subtropical subhumid parts of the state. When the whole range of NSOI and PDO were considered, both the bivariate and trivariate models generated results with almost the same interquartile ranges and basic statistics as the observations. When the data were stratified into different NSOI cases, in the bivariate model, better agreement in the negative NSOI range than in the positive range was noted. It was also found that the inclusion of PDO, in the trivariate model, improved the simulation results, and even better agreement between observations and simulations, in the quadrant which represents negative precipitation anomaly due to La Niña and negative PDO, was observed.

[80] Finally, to validate the copula models, the observation records were divided into two sets: one for modeling, and one for testing and comparing the prediction capabilities of the bivariate and trivariate models. Relatively good correlation between the predicted values and the observations were noted with the bivariate model. The overall coefficient of correlation between observed values and predicted values in the trivariate model was slightly less than with the bivariate model. However, significant improvement was noted in the prediction of negative precipitation anomalies. The trivariate model can thus be effectively used in predicting average negative cold season precipitation anomalies, or drought, based on the state of average June^0–November^0 NSOI and the state of PDO.

[81] From an application perspective it is interesting to note that PDO is a long-term climate variability pattern which shifts phases on at least inter-decadal time scale, usually about 20–30 years. Also, given that average June^0–September^0 NSOI is strongly correlated with average June^0–November^0 NSOI, the former can be used in conjunction with PDO as a forewarning index prior to the start of the hydrologic year.

[82] **Acknowledgments.** C.P.K. was supported by a Dissertation Fellowship from Texas A&M University. We thank H. Chowdhary, S. Feng, J. Huang, and C. Genest for their time and advice on the copula model. We gratefully acknowledge the helpful comments of the Associate Editor, Geoff Pegram, and two anonymous reviewers.

References

Adams, D. K., and A. C. Comrie (1997), The North American monsoon, *Bull. Am. Meteorol. Soc.*, *78*(10), 2197–2213.

Castro, C. L., T. B. McKee, and R. A. Pielke, Sr. (2001), The relationship of the North American monsoon to tropical and North Pacific Sea surface temperatures as revealed by observational analyses, *J. Clim.*, *14*(24), 4449–4473.

Chowdhary, H., L. Escobar, and V. P. Singh (2011), Identification of suitable copulas for bivariate frequency analysis of flood peak and flood volume data, *Hydrol. Res.*, *42*(2–3), 193–216.

Chowdhury, S., and A. Sharma (2009), Multisite seasonal forecast of arid river flows using a dynamic model combination approach, *Water Resour. Res.*, *45*, W10428, doi:10.1029/2008WR007510.

Cole, J. E., J. T. Overpeck, and E. R. Cook (2002), Multiyear La Niña events and persistent drought in the contiguous United States, *Geophys. Res. Lett.*, *29*(13), 1647, doi:10.1029/2001GL013561.

Devineni, N., A. Sankarasubramanian, and S. Ghosh (2008), Multimodel ensembles of streamflow forecasts: Role of predictor state in developing optimal combinations, *Water Resour. Res.*, *44*, W09404, doi:10.1029/2006WR005855.

Embrechts, P., F. Lindskog, and A. McNeil (2003), Modelling dependence with copulas and applications to risk management, in *Handbook of Heavy Tailed Distributions in Finance*, edited by S. T. Rachev, pp. 329–384, Elsevier, Amsterdam, Netherlands.

Fisher, N. I., and P. Switzer (2001), Graphical assessment of dependence: Is a picture worth 100 tests?, *Am. Stat.*, *55*(3), 233–239.

Genest, C., and A.-C. Favre (2007), Everything you always wanted to know about copula modeling but were afraid to ask, *J. Hydrol. Eng.*, *12*(4), 347–368.

Genest, C., J.-F. Quessy, and B. Rémillard (2006), Goodness-of-fit procedures for copula models based on the probability integral transformation, *Scand. J. Stat.*, *33*(2), 337–366.

Genest, C., B. Rémillard, and D. Beaudoin (2009), Goodness-of-fit tests for copulas: A review and a power study, *Insur. Math. Econ.*, *44*(2), 199–213.

Gershunov, A., and T. P. Barnett (1998), Interdecadal modulation of ENSO teleconnections, *Bull. Am. Meteorol. Soc.*, *79*(12), 2715–2725.

Grantz, K., B. Rajagopalan, E. Zagona, and M. Clark (2007), Water management applications of climate-based hydrologic forecasts: Case study of the Truckee-Carson river basin, *J. Water Res. Pl.-ASCE*, *133*(4), 339–350.

Griffiths, J. F., J. W. Zeitler, L. L. Sedlar, D. L. Bjornson, and B. M. Bjornson (1990), *A Decade of Texas Weather (1980–1989) Rep*., 88 pp., Off. of the State Climatol., Dep. of Meteorol., Coll. of Geosci., Texas A&M Univ., College Station, Tex.

Guttman, N. B., and R. G. Quayle (1996), A historical perspective of U.S. climate divisions, *Bull. Am. Meteorol. Soc.*, *77*(2), 293–303.

Ishak, E. H., A. Rahman, S. Westra, A. Sharma, and G. Kuczera (2013), Evaluating the non-stationarity of Australian annual maximum flood, *J. Hydrol.*, *494*(0), 134–145.

Joe, H. (1997), *Multivariate Models and Dependence Concepts*, Chapman and Hall, London, U. K.

Khedun, C. P., A. K. Mishra, J. D. Bolten, H. K. Beaudoing, R. A. Kaiser, J. R. Giardino, and V. P. Singh (2012), Understanding changes in water availability in the Rio Grande/Río Bravo del Norte basin under the influence of large-scale circulation indices using the Noah land surface model, *J. Geophys. Res.*, *117*, D05104, doi:10.1029/2011JD016590.

Kiladis, G. N., and H. van Loon (1988), The southern oscillation. Part VII: Meteorological anomalies over the indian and pacific sectors associated with the extremes of the oscillation, *Mon. Weather Rev.*, *116*(1), 120–136.

Kurtzman, D., and B. R. Scanlon (2007), El Niño-Southern Oscillation and Pacific Decadal Oscillation impacts on precipitation in the southern and central United States: Evaluation of spatial distribution and predictions, *Water Resour. Res.*, *43*, W10427, doi:10.1029/2007WR005863.

Larkin, T. J., and G. W. Bomar (1983), *Climatic Atlas of Texas Rep*., 157 pp., Tex. Dep. of Water Resour., Austin, Tex.

Maity, R., and D. Nagesh Kumar (2008), Probabilistic prediction of hydroclimatic variables with nonparametric quantification of uncertainty, *J. Geophys. Res.*, *113*, D14105, doi:10.1029/2008JD009856.

Mantua, N., and S. Hare (2002), The Pacific Decadal Oscillation, *J. Oceanogr.*, *58*(1), 35–44.

Mantua, N. J., S. R. Hare, Y. Zhang, J. M. Wallace, and R. C. Francis (1997), A Pacific interdecadal climate oscillation with impacts on salmon production, *Bull. Am. Meteorol. Soc.*, *78*(6), 1069–1079.

McCabe, G. J., and M. D. Dettinger (1999), Decadal variations in the strength of ENSO teleconnections with precipitation in the western United States, *Int. J. Climatol.*, *19*(13), 1399–1410.

McGill, R., J. W. Tukey, and W. A. Larsen (1978), Variations of box plots, *Am. Stat.*, *32*(1), 12–16.

McPhaden, M. J., S. E. Zebiak, and M. H. Glantz (2006), ENSO as an integrating concept in earth science, *Science*, *314*(5806), 1740–1745.

Minobe, S. (1997), A 50–70 year climatic oscillation over the North Pacific and North America, *Geophys. Res. Lett.*, *24*(6), 683–686.

Mishra, A. K., V. P. Singh, and M. Özger (2011), Seasonal streamflow extremes in Texas river basins: Uncertainty, trends, and teleconnections, *J. Geophys. Res.*, *116*, D08108, doi:10.1029/2010JD014597.

Nielsen-Gammon, J. W. (2009), The changing climate of Texas, in *The Impact of Global Warming on Texas*, edited by J. Schmandt, J. Clarkson, and G. R. North, Univ. of Tex. Press, Austin.

Özger, M., A. K. Mishra, and V. P. Singh (2009), Low frequency drought variability associated with climate indices, *J. Hydrol.*, *364*(1–2), 152–162.

Pui, A., A. Lal, and A. Sharma (2011), How does the Interdecadal Pacific Oscillation affect design floods in Australia?, *Water Resour. Res.*, *47*, W05554, doi:10.1029/2010WR009420.

Redmond, K. T., and R. W. Koch (1991), Surface climate and streamflow variability in the western United States and their relationship to large-scale circulation indices, *Water Resour. Res.*, *27*(9), 2381–2399.

Rodgers, K. B., P. Friederichs, and M. Latif (2004), Tropical pacific decadal variability and its relation to decadal modulations of ENSO, *J. Clim.*, *17*(19), 3761–3774.

Ropelewski, C. F., and M. S. Halpert (1986), North American precipitation and temperature patterns associated with the El Niño/Southern Oscillation (ENSO), *Mon. Weather Rev.*, *114*(12), 2352–2362.

Ropelewski, C. F., and P. D. Jones (1987), An extension of the Tahiti–Darwin Southern Oscillation index, *Mon. Weather Rev.*, *115*(9), 2161–2165.

SAS/ETS (2011), *User's Guide*, SAS® Publ., Cary, N. C.

Schepsmeier, U., and E. C. Brechmann (2013), Modeling dependence with C- and D-vine copulas: The R package CD vine, *J. Stat. Software*, *52*(3), 1–27.

Sklar, A. (1959), Fonctions de repartition à n dimensions et leurs marges, *Publications de l'Institut de Statistique de l'Université de Paris*, *8*, 229–231.

Trenberth, K. E. (1984), Signal versus noise in the Southern Oscillation, *Mon. Weather Rev.*, *112*(2), 326–332.

Westra, S., and A. Sharma (2010), An upper limit to seasonal rainfall predictability?, *J. Clim.*, *23*(12), 3332–3351.

Wong, G., M. F. Lambert, M. Leonard, and A. V. Metcalfe (2010), Drought analysis using trivariate copulas conditional on climatic states, *J. Hydrol. Eng.*, *15*(2), 129–141.

Yue, S., T. B. M. J. Ouarda, and B. Bobée (2001), A review of bivariate gamma distributions for hydrological application, *J. Hydrol.*, *246*(1–4), 1–18.